Chemical Engineering Journal 535 (2026) 175390

Contents lists available at ScienceDirect

Chemical Engineering Journal

journal homepage: www.elsevier.com/locate/cej

NIR-II excitation light-heat-electric cascade energy conversion nanoparticles for catalytic therapy of colorectal cancer

Baoli Zhou [a,c,1], Ruiyan Li [a,1], Guangkun Song [d], Gaoli Niu [a], Jingwen Han [a], Yongsheng Chen [d], Lingling Xu [b], Xiaoyuan Ji [a], Yong Kang [a,*]

[a] Academy of Medical Engineering and Translational Medicine, Medical College, Tianjin University, Tianjin, 300072, China
[b] School of Nanoscience and Engineering, University of Chinese Academy of Sciences, Beijing, 100049, China
[c] Tianjin The First Hospital, Tianjin, 300232, China
[d] State Key Laboratory and Institute of Elemento-Organic Chemistry, The Centre of Nanoscale Science and Technology and Key Laboratory of Functional Polymer Materials Renewable Energy Conversion and Storage Center (RECAST), Tianjin Key Laboratory of Functional Polymer Materials, College of Chemistry, Nankai University, Tianjin, 300071, China

ARTICLE INFO

Keywords:
Light-heat-electric energy conversion
Photothermal material
Thermoelectric materials
Catalytic therapy
Immunotherapy

ABSTRACT

Colorectal cancer (CRC) is one of the leading causes of cancer-related death worldwide, and treatment is often limited by inadequate energy and drug deposition in deep tissues, as well as difficulty in eradicating deep lesions. Although phototherapy offers high spatial precision and minimal invasiveness, it still faces challenges such as limited tissue penetration and therapeutic resistance, particularly in CRC. To address these limitations, we developed a near-infrared-II (NIR-II)–activated light–heat–electric synergistic nanoplatform (STO@SNPs) that integrates light, heat, and electrical energy conversion for enhanced deep tumor treatment. The platform consists of an organic semiconductor (SKCN) and thermoelectric oxide ($SrTiO_3$, STO), forming a cascaded energy transduction system driven by a single light source. Under 1064 nm irradiation, STO@SNPs exhibit a rapid photothermal response, inducing local temperature gradients and generating significant thermoelectric potential, which drives efficient charge separation and enhances reactive oxygen species (ROS) generation. This synergistic effect induces tumor cell apoptosis and immunogenic cell death (ICD), activating immune responses within the tumor microenvironment. In an orthotopic CRC mouse model, STO@SNPs achieved tumor-targeted accumulation, significantly inhibited tumor growth under NIR-II irradiation, promoted immune modulation, and reduced recurrence and metastasis. This platform offers a promising strategy for the precise and durable treatment of CRC.

1. Introduction

Colorectal cancer (CRC) ranks among the leading causes of morbidity and mortality worldwide and has become one of the most life-threatening malignancies of the digestive system. [1,2] Its complex anatomical structure, abundant stromal components, and the coexistence of hypoxia and immunosuppression severely restrict the diffusion and penetration of therapeutic agents within the tumor microenvironment. [3–5] Consequently, patients with advanced or metastatic CRC derive limited benefit from surgery, radiotherapy, chemotherapy, or single-agent targeted therapies, and recurrence remains frequent. [6] Phototherapy, characterized by its spatial controllability and minimally invasive nature, has emerged as a promising strategy for precise treatment of solid tumors. [7–9] However, conventional photosensitizers exhibit insufficient absorption in the second near-infrared (NIR-II) window. [10–12] Photothermal therapy (PTT) typically requires high temperatures to achieve reliable tumor ablation, which risks collateral tissue damage and induces the upregulation of heat shock proteins. [13,14] In contrast, photodynamic therapy (PDT) relies heavily on oxygen, and the intrinsic hypoxia of deep-seated tumors markedly limits the sustained generation of singlet oxygen and reactive oxygen species (ROS). [15,16] Therefore, achieving a synergistic effect of “low-temperature steady-state heating combined with strong catalytic activity” under deep-penetrating excitation, while effectively converting

* Corresponding author.
E-mail address: kangyong@tju.edu.cn (Y. Kang).
[1] These authors contributed equally to this work.

https://doi.org/10.1016/j.cej.2026.175390
Received 13 January 2026; Received in revised form 11 March 2026; Accepted 18 March 2026
Available online 19 March 2026

localized energy into continuous chemical and immunological cytotoxicity, represents a key scientific challenge in overcoming the therapeutic bottleneck of deep-seated refractory solid tumors.

Inspired by energy-level engineering and intramolecular charge transfer (ICT) concepts in organic photovoltaics, acceptor–donor–acceptor (A-D-A) small molecules, featuring tunable HOMO/LUMO energy-level alignment, strong ICT characteristics, and extended π-conjugation, have emerged as ideal photosensitizing units for achieving efficient light harvesting and nonradiative energy dissipation within the NIR-II window. [17–21] By enhancing ICT strength and modulating excited-state dynamics, A-D-A molecules can narrow the bandgap, broaden infrared absorption, and induce fluorescence quenching, thereby significantly improving photothermal conversion efficiency. [22] Simultaneously, the optimization of spin–orbit coupling and intersystem crossing (ISC) facilitates the generation of reactive species such as superoxide anion radicals ($\cdot O_2^-$) and hydroxyl radical (·OH) even under hypoxic conditions, endowing the system with dual photothermal and photodynamic therapeutic functionalities. [23,24] Furthermore, the incorporation of fully fused-ring and quinoidal configurations enables bond-length homogenization and enhanced π-electron delocalization at the molecular level, which collectively increase the NIR-II extinction coefficient and molecular rigidity, extend the excited-state lifetime, and suppress conformational vibrational losses. [22] These structural refinements also strengthen energy and electron transfer to oxygen, thereby amplifying ROS production while maintaining mild irradiation conditions and reducing thermal thresholds that typically constrain therapeutic efficacy. [25] Representative A-D-A molecules derived from quinoline-fused BTP (Y6) backbones have demonstrated outstanding photothermal conversion efficiency and radical-generating activity under 1064 nm excitation, providing a solid material foundation for NIR-II–driven dual-mode phototherapy of deep-seated solid tumors. [26,27]

However, despite possessing strong NIR-II absorption and dual-mode photocatalytic capability, a single-step "light-to-heat" or "light-to-ROS" energy conversion remains insufficient to achieve sustained and robust chemical cytotoxicity within the complex tumor microenvironment. First, most of the absorbed light energy is rapidly dissipated as transient heat, resulting in poor energy utilization and limited therapeutic persistence. [28–30] Second, ROS generation remains highly dependent on oxygen availability, leading to markedly reduced efficacy in hypoxic tumors. [31,32] To further improve energy-conversion efficiency and therapeutic stability, "energy-cascade" and "multi-field coupling" strategies were implemented, whereby rational materials engineering enables a single external stimulus to be sequentially transformed in vivo into heat, charge carriers, and reactive radicals, thus maximizing energy utilization and achieving multidimensional amplification of therapeutic effects. Owing to their unique thermoelectric effect, thermoelectric oxides and other inorganic components can generate considerable internal electric potential under temperature difference drive, thereby driving the directional migration of charges and interface redox reactions and providing a new energy channel for constructing the "heat→electricity→chemistry" cascade killing process. For example, strontium titanate ($SrTiO_3$, STO) can generate pronounced Seebeck potentials under external thermal stimulation, driving directional electron–hole migration and facilitating redox reactions. [33,34] This multistage conversion mechanism effectively overcomes the limitations of traditional photocatalysis-such as the short lifetime of excited states and oxygen dependence-thus providing a new energy-driving paradigm for catalytic cancer therapy. As a representative wide-bandgap n-type thermoelectric semiconductor, STO exhibits high carrier mobility, excellent chemical stability, and outstanding thermoelectric responsiveness. [35] Its large Seebeck coefficient enables the generation of substantial internal electric potentials even under small temperature gradients, thereby driving electron flow and enhancing electrocatalytic processes. [36–38] In addition, interfacial polarization within STO stabilizes carrier migration pathways, minimizes energy dissipation, and suppresses parasitic reactions, ensuring durable catalytic stability under prolonged photoirradiation. [25,39]

Grounded in the foregoing theoretical and materials framework, we engineered an NIR-II-activated light-heat-electric cascaded nanoplatform (SKCN/STO), thereby advancing a three-stage "light-heat-electric" energy-coupling paradigm. In this construct, SKCN-a quinoidal A-D-A photosensitizer-affords strong NIR-II absorption and high photothermal conversion efficiency, enabling efficient photon harvesting and the establishment of a stable, moderate-temperature thermal field under NIR-II irradiation. STO, which functions as a thermoelectric semiconductor, forms an intimate heterointerface with SKCN and, upon photothermal stimulation, generates a substantive thermoelectric potential via the Seebeck effect on the STO side, which in turn drives carrier separation and interfacial electrocatalysis. The resulting built-in field orchestrates interfacial separation and directed migration of photo/thermally induced carriers: excited electrons preferentially engage in O_2 reduction to produce $\cdot O_2^-$, whereas holes catalyze H_2O to yield ·OH, thereby sustaining type I/II ROS generation under a mild-thermal operating regime. In an orthotopic colorectal cancer model, the SKCN/STO platform achieves tumor-selective accumulation through the enhanced permeability and retention (EPR) effect and elicits robust antitumor efficacy with pronounced immune activation, as evidenced by dendritic cell maturation, M1-like macrophage polarization, and cytotoxic T lymphocyte activation, collectively remodeling the tumor immune microenvironment and suppressing recurrence and metastasis (Fig. 1). Overall, this work delineates a multistage "light → heat → electric → chemical → immune" energy-transduction cascade and provides a rigorous mechanistic basis and practicable technological route for deploying thermoelectric catalytic materials in oncologic therapy.

2. Materials and methods

2.1. Preparation of thermoelectric material $SrTiO_3$ (STO)

Nanostructured $SrTiO_3$ (STO) was synthesized via a rapid sol–gel precipitation method. Specifically, 16 mmol of titanium butoxide ($Ti(OBu)_4$), 16 mmol of strontium hydroxide octahydrate ($Sr(OH)_2{\cdot}8H_2O$), 0.74 g of polyvinylpyrrolidone (PVP, K30), and 8 mL of ammonium hydroxide solution (25–28%) were dissolved in 40 mL of triethylene glycol (TEG). The mixture was heated to 160 °C and stirred for 2 h. After natural cooling, a yellow, transparent, and highly stable sol was obtained. The sol was precipitated using deionized water, and the resulting product was separated and washed thoroughly with deionized water and ethanol to yield STO.

2.2. Preparation of SKCN

Malononitrile (46 mg, 0.70 mmol) was dissolved in tetrahydrofuran (THF, 5 mL) and slowly added to sodium hydride (60% in oil, 40 mg, 1 mmol) at 0 °C. The reaction mixture was stirred at room temperature for 1 h, followed by the addition of compound 1 (200 mg, 0.18 mmol) and tetrakis (triphenylphosphine) palladium (41.6 mg, 0.036 mmol). The mixture was heated to 70 °C for 8 h and then quenched with diluted hydrochloric acid (2 M, 10 mL) while cooling in an ice bath. The resulting solution was extracted with dichloromethane, followed by the addition of 2,3-Dichloro-5,6-dicyano-1,4-benzoquinone (DDQ) (81 mg, 0.36 mmol). After stirring at room temperature for 1 h, the mixture was poured into water and extracted twice with chloroform (30 mL × 2). The combined organic layers were dried over anhydrous $MgSO_4$, and the solvent was removed under reduced pressure. The crude product was purified by silica gel column chromatography, followed by recrystallization from a chloroform/methanol mixture to afford a dark green solid SKCN (106 mg, 54% yield).

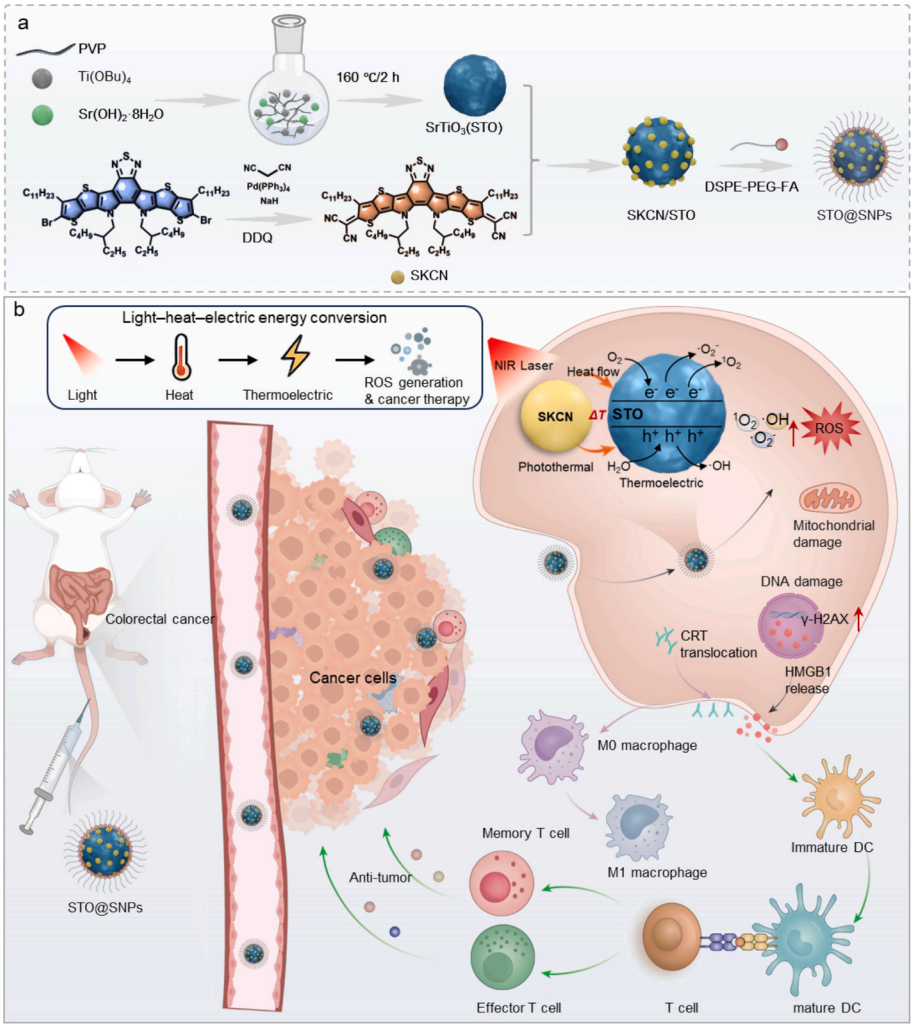

Fig. 1. Schematic illustration of NIR-II photothermal-electrocatalytic therapy of colorectal cancer using STO@SNPs nanoparticles. (a) Synthesis of STO@SNPs nanoparticles. (b) Under 1064 nm laser irradiation, STO@SNPs nanoparticles induce tumor cell apoptosis through a photothermal-electrocatalytic cascade. The treatment promotes the release of tumor antigens and damage-associated molecular patterns (DAMPs), enhancing dendritic cell maturation and M1 polarization of macrophages, thereby effectively treating primary colorectal tumors.

2.3. Preparation of STO, SNPs, and STO@SNPs nanoparticles

STO, SNPs, and STO@SNPs nanoparticles were fabricated via a nanoprecipitation method. Briefly, 20 mg of DSPE-PEG-FA was dissolved in 1 mL of THF. Separately, 0.5 mg of SKCN and 0.5 mg of STO were dissolved in 1 mL of THF. Both solutions were sonicated in a water bath for 5 min and then mixed. The mixed solution was immediately added to 10 mL of a water–THF mixture (*v*/v = 9:1) and sonicated for an additional 15 min. The resulting dispersion was gently shaken overnight to evaporate THF. The solution was filtered through a 0.45 μm membrane and centrifuged three times with ultrapure water using a Millipore ultrafiltration tube. The supernatant containing STO@SNPs nanoparticles was collected. The concentration of the nanoparticles was determined based on their UV–vis absorption peaks and calibration curves. STO nanoparticles were prepared by mixing STO with DSPE–PEG-FA under identical conditions, while SNPs nanoparticles were obtained by mixing SKCN with DSPE-PEG-FA.

2.4. Structural characterization

The morphologies of STO, SNPs, and STO@SNPs nanoparticles were examined using transmission electron microscopy (TEM). The zeta potential and hydrodynamic diameters were measured using a laser particle size analyzer.

2.5. Photothermal performance evaluation

The temperature variation and thermal imaging of SNPs solutions at different concentrations (0, 5, 12.5, 25, and 50 μg/mL) were recorded using an infrared thermal imaging camera under 1064 nm laser irradiation with a power density of 1.0 W/cm^2. Corresponding temperature–time profiles were plotted. In addition, SNPs solutions at a concentration of 50 μg/mL were irradiated under different power densities (0, 0.5, 1.0, and 1.5 W/cm^2), and the resulting temperature changes and thermal images were similarly recorded to generate temperature evolution curves.

The photothermal conversion efficiency of SNPs was calculated as follows: photothermal conversion efficiency$(\eta) = \frac{hA(T_{max}-T_{surr})-Q_s}{I(1-10^{-A_{1064}})}$. I in the equation is the laser density and A_{1064} is the UV absorbance of SNPs at 1064 nm. Qs is the heat associated with the light absorbance of the water. T_{max} is the maximum temperature change and T_{surr} is the temperature of ambient. To get hA, θ defined as the ratio of (T-T_{surr}) to (T_{max}-T_{surr}) is introduced. T was the system temperature. Therefore, hA could be calculated by the linear time data from the cooling period vs $-ln\theta$: $t = -\frac{\sum_i m_i C_{p,i}}{hA} ln\theta$. m in the equation is the mass of solvent (water) and Cp is

the heat capacity of solvent (water). Then, the photothermal conversion efficiency (η) of SNPs could be calculated. [40,41]

2.6. In vitro catalytic performance evaluation

The generation of ROS by STO, SNPs, and STO@SNPs under 1064 nm laser irradiation was evaluated using DPBF and ABDA as probe molecules. For the DPBF assay, a DPBF stock solution (2 mg/mL, 230 μM) was prepared. Different concentrations of STO@SNPs (0, 12.5, 25, 50, and 75 μg/mL) were mixed with DPBF and irradiated with a 1064 nm laser (1.5 W/cm^2). The UV absorbance at 420 nm was recorded every 5 min for 25 min, and the changes were plotted as absorption decay curves. In a separate test, STO@SNPs (50 μg/mL) was exposed to laser irradiation at various power densities (0, 0.5, 1.0, and 1.5 W/cm^2), and the absorbance at 420 nm was similarly monitored every 5 min over 25 min. For the ABDA assay, an ABDA stock solution (2 mg/mL, 160 μM) was prepared. Mixtures containing different concentrations of STO@SNPs (0, 25, 50, and 75 μg/mL) were irradiated with a 1064 nm laser (1.0 W/cm^2). The absorbance at 400 nm was recorded every 5 min for 25 min to track the ROS-mediated degradation of ABDA. Additionally, STO@SNPs (50 μg/mL) was subjected to different power densities (0, 0.5, 1.0, and 1.5 W/cm^2) under the same wavelength, and absorbance at 400 nm was monitored over 25 min. The catalytic activity of pure STO and SNPs was evaluated following the same protocol.

The thermoelectric activation properties of STO materials were measured by electrochemical method. The current-time response of STO under temperature variation was investigated using a CHI 920d electrochemical workstation in a standard three-electrode system. The system employed a glassy carbon electrode as the working electrode, Ag/AgCl as the reference electrode, and a platinum wire as the auxiliary electrode, with phosphate-buffered saline (PBS) as the electrolyte. A suspension of STO (100 μL) was dropped onto the surface of the glassy carbon electrode and dried at room temperature. Subsequently, the current generated by the pyroelectric effect of STO was measured in chronoamperometric mode under conditions with and without temperature variation.

2.7. Biocompatibility evaluation

The cytotoxicity of STO@SNPs nanoparticles was assessed in NCM460 and CT26 cells. Cells were seeded into 96-well plates at a density of 1×10^4 cells per well and incubated for 12 h. The medium was then replaced with fresh medium containing various concentrations of STO@SNPs, followed by 24 h of incubation. Afterward, CCK-8 reagent was added to each well and incubated for 2 h. The cell viability was determined by measuring absorbance at 450 nm, indicating the biocompatibility of STO@SNPs.

Furthermore, the combined effects of STO, SNPs, and STO@SNPs with 1064 nm laser irradiation on CT26 cell viability were also evaluated. CT26 cells were incubated with different concentrations of each sample for 12 h, followed by irradiation with a 1064 nm laser (1.0 W/cm^2) for 5 min per well. After another 12 h of incubation, cell viability was quantified using the CCK-8 assay.

2.8. In vitro light-induced ROS generation by STO@SNPs

Intracellular ROS generation induced by STO@SNPs under 1064 nm laser irradiation was analyzed using DCFH-DA as a fluorescent probe via fluorescence microscopy and flow cytometry (FCM). CT26 cells were seeded into 12-well plates at a density of 2×10^5 cells per well and incubated for 12 h. The experimental groups included: Control, L (laser only), STO@SNPs, STO + L, SNPs + L, and STO@SNPs + L. The concentrations of STO, SNPs, and STO@SNPs were fixed at 50 μg/mL. After replacing the culture medium, cells were further incubated for 12 h and washed twice with PBS. Then, 0.2 μM DCFH-DA was added, and cells were incubated at 37 °C for 30 min. For light-treated groups, cells were irradiated with a 1064 nm laser at 1.0 W/cm^2 for 5 min. After washing with PBS, ROS generation was visualized by fluorescence microscopy and quantified by flow cytometry. FCM data were analyzed using FlowJo v10.9.0 software.

2.9. In vitro antitumor evaluation

To assess early DNA damage in CT26 cells induced by STO@SNPs under 1064 nm laser irradiation, phosphorylated histone H2AX (Ser139) was used as a biomarker and analyzed via immunofluorescence staining. CT26 cells were seeded into confocal culture dishes at a density of 2×10^5 cells per dish and incubated for 12 h. The experiment included six groups: Control, L (laser only), STO@SNPs, STO + L, SNPs + L, and STO@SNPs + L, with STO, SNPs, and STO@SNPs concentrations fixed at 50 μg/mL. After replacing the medium, cells were incubated for another 12 h. For the laser treatment groups, cells were irradiated with a 1064 nm laser (1.0 W/cm^2), targeting five regions per dish with 5 min of exposure per region. Two hours after irradiation, cells were washed with PBS and stained with a phosphorylated histone H2AX (Ser139) antibody for 30 min, followed by three PBS washes. Phosphorylated H2AX (γ-H2AX) expression was visualized using CLSM to evaluate DNA damage under different treatment conditions.

Cell viability was assessed using the Calcein-AM/PI assay. CT26 cells were seeded into 12-well plates (2×10^5 cells/well) and incubated for 12 h. The experiment included six groups: Control, L, STO@SNPs, STO + L, SNPs + L, and STO@SNPs + L, with STO, SNPs, and STO@SNPs concentrations fixed at 100 μg/mL. The cells were incubated with different materials for 12 h. For laser-treated groups, cells were irradiated with a 1064 nm laser (1.0 W/cm^2) for 5 min. Two hours post-treatment, cells were stained with a Calcein-AM/PI mixture for 30 min, washed twice with PBS, and observed under a fluorescence microscope to distinguish live (green) and dead (red) cells. Following identical treatments, apoptosis in CT26 cells was evaluated using an Annexin V-FITC apoptosis detection kit and quantified via FCM. Data were analyzed using FlowJo v10.9.0 software.

For HSP70 expression analysis, CT26 cells were seeded into confocal culture dishes at a density of 2×10^5 cells per dish and incubated for 12 h. The experiment included six groups: Control, L, STO@SNPs, STO + L, SNPs + L, and STO@SNPs + L, with STO, SNPs, and STO@SNPs concentrations fixed at 50 μg/mL. After replacing the medium, cells were incubated for another 12 h. For the laser treatment groups, cells were irradiated with a 1064 nm laser (1.0 W/cm^2), targeting five regions per dish with 5 min of exposure per region. Two hours after irradiation, cells were washed with PBS, stained with HSP70 antibody, and the expression level of HSP70 was observed using a CLSM.

To further investigate the motion of STO@SNPs, three-dimensional (3D) cellular spheroids based on CT26 cells were established. Specifically, each well of a 96-well plate was first filled with 50 μL of 1% agarose, which was then exposed to UV light for at least 30 min prior to use. Subsequently, 200 μL of CT26 cell suspension (1×10^3 cells) was added to each well and incubated for 7 days to form 3D cellular spheroids. FITC-conjugated STO@SNPs were added to each well. After a 6-h incubation period, the 3D cellular spheroids were removed from the wells and washed three times with PBS. CLSM was employed to examine the 3D cellular spheroids after various treatments.

2.10. In vitro immunogenic cell death (ICD) evaluation

To investigate the induction of immunogenic cell death, the expression of calreticulin (CRT) on CT26 cells was examined. CT26 cells were seeded in confocal culture dishes at a density of 2×10^5 cells/dish and incubated for 12 h. Six groups were included: Control, L, STO@SNPs, STO + L, SNPs + L, and STO@SNPs + L, with each treatment at 50 μg/mL. After replacing the culture medium, cells were incubated for another 12 h. For laser-treated groups, cells were irradiated with a 1064 nm laser (1.0 W/cm^2) for 5 min at five points per dish.

Two hours later, cells were incubated with an anti-CRT antibody (1:200 dilution). CRT expression was visualized using CLSM to evaluate the ICD-inducing capability of different treatments.

2.11. In vitro dendritic cell (DC) activation by light-controlled nanoparticles (STO@SNPs)

Bone marrow cells were harvested from the tibias and femurs of 6-week-old BALB/c mice and cultured in 12-well plates. Granulocyte-macrophage colony-stimulating factor (GM-CSF) and interleukin-4 (IL-4) were added to induce differentiation into bone marrow-derived dendritic cells (BMDCs). After 6 days of culture, immature dendritic cells were transferred to the lower chamber of a transwell system, while CT26 cells were seeded into the upper chamber. The six experimental groups were as follows: Control, L, STO@SNPs, STO + L, SNPs + L, and STO@SNPs + L, each with 50 μg/mL of STO, SNPs, or STO@SNPs. For laser-treated groups, each well was irradiated with a 1064 nm laser (1.0 W/cm^2) for 5 min. After laser exposure, cells in both chambers were co-cultured for 24 h. The lower-chamber DCs were then collected and stained with anti-CD11c, anti-CD80, and anti-CD86 antibodies. DC activation was analyzed by FCM, and data were processed using FlowJo v10.9.0 software.

2.12. In vitro T cell activation

Spleens were collected from healthy 6-week-old BALB/c mice, mechanically dissociated, and treated with red blood cell lysis buffer to isolate T cells. Purified T cells were stimulated with anti-CD3 and anti-CD28 antibodies and cultured for three days. The activated T cells were then transferred to the lower chamber of a transwell system, while CT26 cells were seeded in the upper chamber. Experimental groups were identical to those described above (Control, L, STO@SNPs, STO + L, SNPs + L, STO@SNPs + L; all at 50 μg/mL). After 12 h, the L groups were irradiated with a 1064 nm laser (1.0 W/cm^2) for 5 min. Cells in both chambers were co-cultured for an additional 24 h. Subsequently, T cells were collected and stained with anti-CD3, anti-CD4, and anti-CD8 antibodies, followed by FCM analysis. Data were processed using FlowJo v10.9.0 software.

2.13. Establishment of orthotopic rectal tumor model in mice

Female BALB/c mice (7 weeks old, 15–17 g) were anesthetized, and their anal region was gently dilated using a retractor to expose the rectum. CT26-luc cells (3×10^6 cells per mouse) were injected into the rectal wall using a 30-gauge needle to establish the orthotopic rectal tumor model. Tumor progression and therapeutic responses were monitored using an in vivo imaging system (IVIS, PerkinElmer).

2.14. In vivo antitumor evaluation

To evaluate the targeting ability of the constructed drug to tumor tissues, ICG was coated onto the surface of STO@SNPs to form an ICG-STO@SNPs complex with fluorescence properties. Then, this complex was injected into mice via the tail vein. The fluorescence intensity of the tumors was observed at 1, 2, 5, 8, 12, and 24 h after injection. And the mice were euthanized at 1, 3, 8 and 24 h to evaluate the fluorescence intensity in the major organs and the tumor site. Plasma pharmacokinetics of STO@SNPs after intravenous administration was evaluated by ICP-MS using Sr as the elemental tracer, since STO@SNPs contain $SrTiO_3$. The Sr content in lyophilized STO@SNPs was determined in advance to establish the conversion factor between nanoparticle mass and elemental Sr amount. Female BALB/c mice received STO@SNPs via tail-vein injection at 5 mg/kg in a total volume of 200 μL. Blood samples was collected at 5 min, 15 min, 30 min, 1, 2, 4, 6, 8, 12, 24, and 48 h after injection, and plasma was isolated. Plasma samples was digested with nitric acid/hydrogen peroxide and analyzed for Sr content by ICP-MS. Pharmacokinetic parameters was calculated using non-compartmental analysis. Plasma from untreated mice will be used as the blank matrix for background correction.

Following successful establishment of the orthotopic rectal tumor model, tumor growth was monitored via IVIS imaging. Mice were anesthetized with isoflurane and injected intraperitoneally with D-luciferin (150 mg/kg) for bioluminescence imaging. Treatments began on day 7 post-cell inoculation. Mice were randomly divided into six groups: Control, L, STO@SNPs, STO + L, SNPs + L, and STO@SNPs + L. All treatment groups received intravenous injections (200 μL total volume) of STO, SNPs, or STO@SNPs at a dose of 5 mg/kg. Eight hours post-injection, mice in the laser-treated groups were irradiated at the tumor site with a 1064 nm laser (0.7 W/cm^2) for 8 min. Infrared thermal imaging was used to monitor and record temperature changes in the tumor region. The same treatment was repeated on day 3. Tumor growth was monitored by IVIS imaging, and body weight was recorded every two days. On day 9, mice were euthanized, and colorectal tissues and tumors were collected. Tumor sections were analyzed by hematoxylin and eosin (H&E) staining and TUNEL assay to evaluate histopathological changes and apoptosis.

2.15. In vivo immune response evaluation

To assess systemic immune responses, mice were euthanized on day 9 post-treatment, and tumors, spleens, and lymph nodes were collected for flow cytometric analysis. Lymph nodes were ground to obtain single-cell suspensions, while spleens were mechanically dissociated and treated with red blood cell lysis buffer. Tumor tissues were minced and enzymatically digested with type IV collagenase and DNase I at 37 °C for 1 h, filtered through 70 μm strainers, and processed for red blood cell lysis. Single-cell suspensions were stained with fluorophore-conjugated monoclonal antibodies, including anti-CD45, anti-CD3, anti-CD4, anti-CD8a, anti-CD11c, anti-CD80, and anti-CD86. Immune cell populations were analyzed via FCM, and data were processed using FlowJo v10.9.0 software.

2.16. In vivo biosafety evaluation

To evaluate the biosafety of STO@SNPs treatment in mice with orthotopic rectal tumors, body weights were continuously recorded during the therapeutic period. On day 9, mice were euthanized, and major organs—including the heart, liver, spleen, lungs, and kidneys—were collected. The organs were subjected to H&E staining for histological examination to assess potential morphological or pathological changes. In addition, to comprehensively evaluate the potential systemic toxicity induced by the administered formulations, blood samples were collected from mice in each group at day 9 post-injection. Subsequently, hematological analysis (Hematocrit (HCT), Hemoglobin (HGB), Mean Corpuscular Hemoglobin (MCH), Mean Corpuscular Hemoglobin Concentration (MCHC), Mean Corpuscular Volume (MCV), Red Blood Cell count (RBC), and White Blood Cell count (WBC)) and serum biochemical (Albumin (ALB), Alanine Aminotransferase (ALT), Amylase (AMY), Aspartate Aminotransferase (AST), Blood Urea Nitrogen (BUN), Creatine Phosphokinase (CK), Lactate Dehydrogenase (LDH), Total Protein (TP)) assays were performed to assess possible alterations in blood parameters and organ function.

3. Results

3.1. Preparation and characterization of light-responsive STO@SNPs

Nanostructured STO was synthesized via a rapid sol–gel precipitation method using titanium butoxide, strontium hydroxide, polyvinylpyrrolidone (PVP), ammonium hydroxide, and triethylene glycol. The quinoidal molecule SKCN was synthesized by 2, 10-dibromo-12, 13-bis (2-ethylhexyl)-3, 9-diundecyl-12, 13-dihydro-[1,2,5] thiadiazolo

[3,4-e] thieno [2′‘,3′”:4′,5′] thieno [2′,3′:4,5] pyrrolo [3,2-g] thieno [2′,3′:4,5] thieno [3,2-b] indole coupling with malononitrile and then oxidized by DDQ, The STO@SNPs nanoparticles were composed of STO and SKCN as the core components and coated with 1,2-distearoyl-sn-glycero-3-phosphoethanolamine-N-folate(polyethylene glycol) (DSPE-PEG-FA). Such PEGylation imparted excellent colloidal stability, uniform dispersibility, and improved biocompatibility to the nanoparticles, thereby effectively extending their systemic circulation time in vivo (Fig. 1a).

Transmission electron microscopy (TEM) images demonstrated that STO, and SNPs exhibited uniform and well-dispersed spherical morphologies with an average diameter of around 100 nm, while STO@SNPs showed a slightly increased particle size compared with the individual components (Fig. 2a-c). Consistently, dynamic light scattering analysis revealed hydrodynamic diameters of 105 nm, 91 nm, and 122 nm for STO, SNPs, and STO@SNPs, respectively (Fig. 2d). Zeta

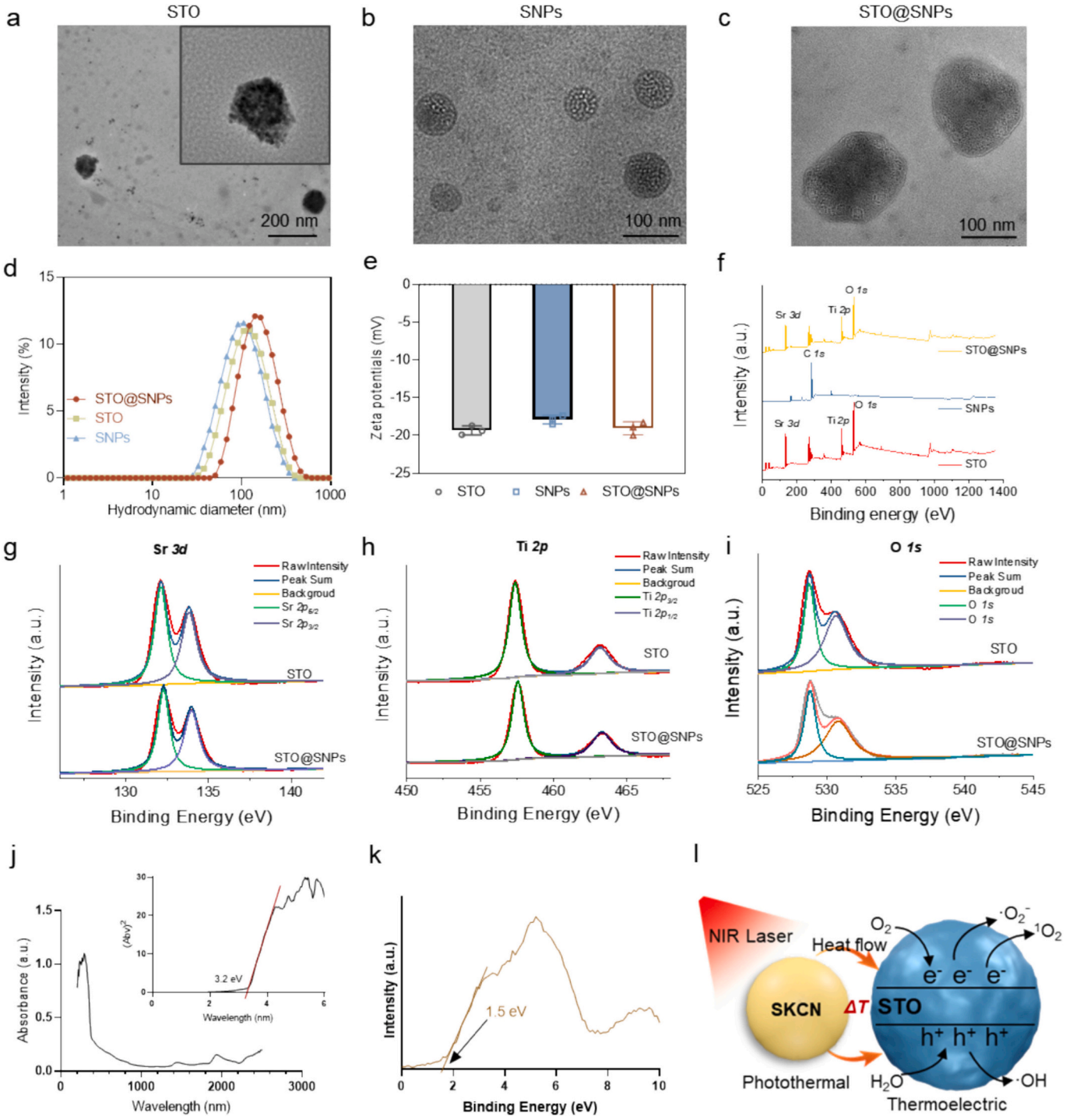

Fig. 2. Preparation and Characterization of STO@SNPs. (a) TEM image of STO, Scale bar = 200 nm. (b) TEM image of SNPs, Scale bar = 100 nm; (c) TEM images of the STO@SNPs, Scale bar = 100 nm. (d) Particle size distributions of STO, SNPs and STO@SNPs. (e) Zeta potential of STO, SNPs and STO@SNPs. (f) XPS spectra of the STO, SNPs and STO@SNPs. (g) XPS spectra of Sr 3d of STO and STO@SNPs. (h) XPS spectra of Ti 2p of STO and STO@SNPs. (i) XPS spectra of O 1s of STO and STO@SNPs. (j) UV–vis absorbance spectra and calculated band gap of STO. (k) Calculated VB of STO from XPS spectra. (j) Mechanism of the light-heat-electric cascade energy conversion nanoparticles.

potential measurements further confirmed that all nanoparticles carried negative surface charges, with STO, SNPs, and STO@SNPs showing values of −18.7 mV, −17.4 mV, and − 18.3 mV, respectively (Fig. 2e). The appropriate particle size and moderate negative surface potential of STO@SNPs are expected to facilitate prolonged systemic circulation and improved accumulation within tumor tissues. The infrared absorption spectra (Fig. S1) demonstrated that both SNPs and STO@SNPs exhibit pronounced absorption in the 800–1150 nm region, with the cutoff wavelength extending beyond 1400 nm. This broad and intense absorption confirms that the modification preserves the intrinsic NIR-II light-harvesting capability, providing a favorable optical foundation for subsequent photothermal and photoelectronic applications. To further evaluate the long-term stability of STO@SNPs, dynamic light scattering (DLS) analysis was conducted for 14 days (Fig. S2). The particle size distribution profiles obtained at different time points showed substantial overlap and comparable peak positions, indicating that the hydrodynamic diameter of STO@SNPs remained essentially unchanged during storage. No apparent aggregation or instability was observed, confirming the favorable long-term stability of STO@SNPs.

We employed X-ray photoelectron spectroscopy (XPS) to assess the chemical composition of STO, SNPs, and STO@SNPs. The STO XPS spectrum reveals signals corresponding to Ti, Sr, and O, consistent with the STO composition. In contrast, the SNPs spectrum shows a prominent presence of carbon, indicating substantial carbon-based species. The STO@SNPs spectrum contains signals from Ti, Sr, and O, confirming the presence of STO in the composite (Fig. 2f). In addition, detailed analyses were conducted on the typical high-resolution XPS spectra of Sr 3d, Ti 2p, O 1s, and C 1s in STO, SNPs, and STO@SNPs. Specifically, in the high-resolution XPS spectrum of STO and STO@SNPs (Fig. 2g-i), lines such as Sr 2p5/2, Sr 2p3/2, Ti 2p3/2, Ti 2p1/2, and O 1s were observed. Meanwhile, lines such as sp2/sp3 C, C—O, C═O, and O-C=O were observed in the high-resolution XPS spectrum of SNPs and STO@SNPs (Fig. S3). Overall, these results indicate the successful preparation of the thermoelectric material STO NSs and the self-igniting thermoelectric system STO@SNPs.

To investigate the light-heat-electric multi-mode catalytic mechanism mediated by STO@SNPs under laser irradiation, we performed a detailed characterization of the band structure, including the conduction band (CB) and valence band (VB) edge positions and the band gap (Eg). The band structure was probed by diffuse reflectance spectroscopy (DRS) and XPS analyses. First, we analyzed the DRS spectra of STO. From these analyses, the Eg values estimated by the Kubelka-Munk (K-M) method are 3.2 eV for STO (Fig. 2j). The VB positions obtained from XPS are 1.5 eV for STO (Fig. 2k). Accordingly, the CB edge positions, calculated by subtracting their Eg values from the VB positions, are calculated to be −1.7 eV for STO, which is more negative than the redox potential of $O_2/\cdot O_2^-$. The electronic structure characteristics of STO make it an excellent oxygen reduction catalyst and ROS generation catalyst. Specifically, when STO@SNPs nanosheets enter the tumor microenvironment, the SNPs nanoparticles release a large amount of heat under laser irradiation. The heat-induced temperature difference triggers the thermal catalytic effect of STO, causing the separation of electrons and holes, and transforming them into the conduction CB of STO. Moreover, as the temperature difference is generated, an electric potential difference is formed between the hot end and the cold end, causing negative charges to flow from the hot end of the material to the cold end. Due to the presence of the thermoelectric potential, the band energy on the negative potential side increases, while the band energy on the positive potential side decreases. Therefore, the band energy of the entire material tilts, with the CB position approaching the redox potential required for the generation of $\cdot O_2^-$, and the VB position approaching the redox potential required for the generation of ·OH. As a result, STO nanomaterials generate $\cdot O_2^-$, $^1O_2$, and ·OH under thermal excitation (Fig. 2l).

3.2. Light-heat-electric catalytic performance

The photothermal performance of SNPs was systematically evaluated using infrared thermal imaging. Under 1064 nm laser irradiation at a power density of 1.0 W cm^{-2}, the temperature evolution of SNPs solutions at different concentrations was recorded. As shown in the thermal images (Fig. 3a) and heating curves (Fig. 3b), a 50 μg/mL SNPs solution rapidly increased to 55.7 °C within 10 min, while even at the lowest concentration (5 μg/mL), the temperature reached 44.8 °C. In contrast, the PBS control showed only a minimal temperature increase from 26.5 °C to 29.7 °C under the same conditions. Furthermore, the 50 μg/mL SNPs solution was subjected to 1064 nm laser irradiation at varying power densities. The heating curves (Fig. 3c) indicated that the solution reached 45.9 °C after 10 min even at a low power density of 0.5 W cm^{-2}, and achieved a maximum temperature of 61.1 °C at 1.5 W cm^{-2}. These results highlight the excellent photothermal potential of SNPs, which can be attributed to its quinonoid A–D–A structure incorporating a BTP core, significantly enhancing intramolecular charge transfer (ICT) and thereby enabling highly efficient photothermal conversion. To assess the persistence of the photothermal effect, a 50 μg/mL SNPs solution was subjected to 5 consecutive heating-cooling cycles under a 1064 nm laser irradiation with intensity of 1.5 W cm^{-2}. During each cycle, the temperature always exceeds 62 °C and quickly returns to room temperature after the laser is turned off (Fig. 3d). Many infrared molecules rely on olefin bonds to maintain conjugation, and they are prone to photoisomerization or photooxidation under light. While, SNPs expands conjugation by fusing ring structures, not only enhancing the molecular rigidity but also significantly improving the molecular stability. This structural advantage ensures that SNPs remains stable under long-term laser irradiation and maintains its properties and reactivity during phototherapy. According to the formula, the photothermal conversion efficiency (η) of SNPs was calculated to be 72.3%, further confirming the excellent photothermal conversion efficiency of SNPs (Fig. 3e, f). To further assess the stability of STO@SNPs under repeated laser irradiation, a 50 μg/mL STO@SNPs solution was subjected to five consecutive heating-cooling cycles under 1.5 W cm^{-2} 1064 nm laser irradiation. The temperature rise and fall data of the solution were recorded. As shown in Fig. S4, during the five continuous cycles of laser irradiation, the temperature rise performance of STO@SNPs remained stable, indicating that the material possesses excellent thermal stability.

The ROS generation capability of STO, SNPs, and STO@SNPs under 1064 nm laser irradiation was systematically evaluated using 1,3-diphenylisobenzofuran (DPBF) as a probe for detecting $\cdot O_2^-$ and singlet oxygen ($^1O_2$). DPBF exhibited a gradual decrease in absorption at 420 nm upon laser irradiation with laser intensity of 1.5 W cm^{-2}. Specifically, the absorption intensity decreased to 64.5%, 43.7%, and 33.1% at a concentration of 75 μg/mL for STO, SNPs, and STO@SNPs, respectively. Statistical analysis showed that the ability of STO@SNPs group to produce ROS was significantly stronger than that of STO and SNPs groups (Fig. 3g, Fig. S5). Also, Fig. S6 exhibited that the amount of ROS production increased with increasing nanoparticle concentration, laser power, and exposure time. Notably, the STO solution generated a small amount of ROS upon laser illumination, which could be attributed to a slight temperature increase in the STO solution caused by laser radiation. This temperature rise likely activated the STO, leading to ROS production and demonstrating the material's effective thermal excitation capacity. However, the ROS generated by STO alone under laser irradiation was minimal in comparison to the significantly higher ROS production observed in the SNPs and STO@SNPs groups. Under the same conditions, the $^1O_2$ generation capability of the materials was evaluated using 9,10-anthracenediyl-bis(methylene) dimalonic acid (ABDA) as a probe. At a SNPs concentration of 50 μg/mL, the absorption peak of ABDA at 400 nm decreased to 59%, indicating that SNPs exhibits a high ROS generation efficiency under 1064 nm laser irradiation, thereby significantly enhancing NIR-II photodynamic therapy performance. For the STO@SNPs, the ABDA absorption at 400 nm decreased to

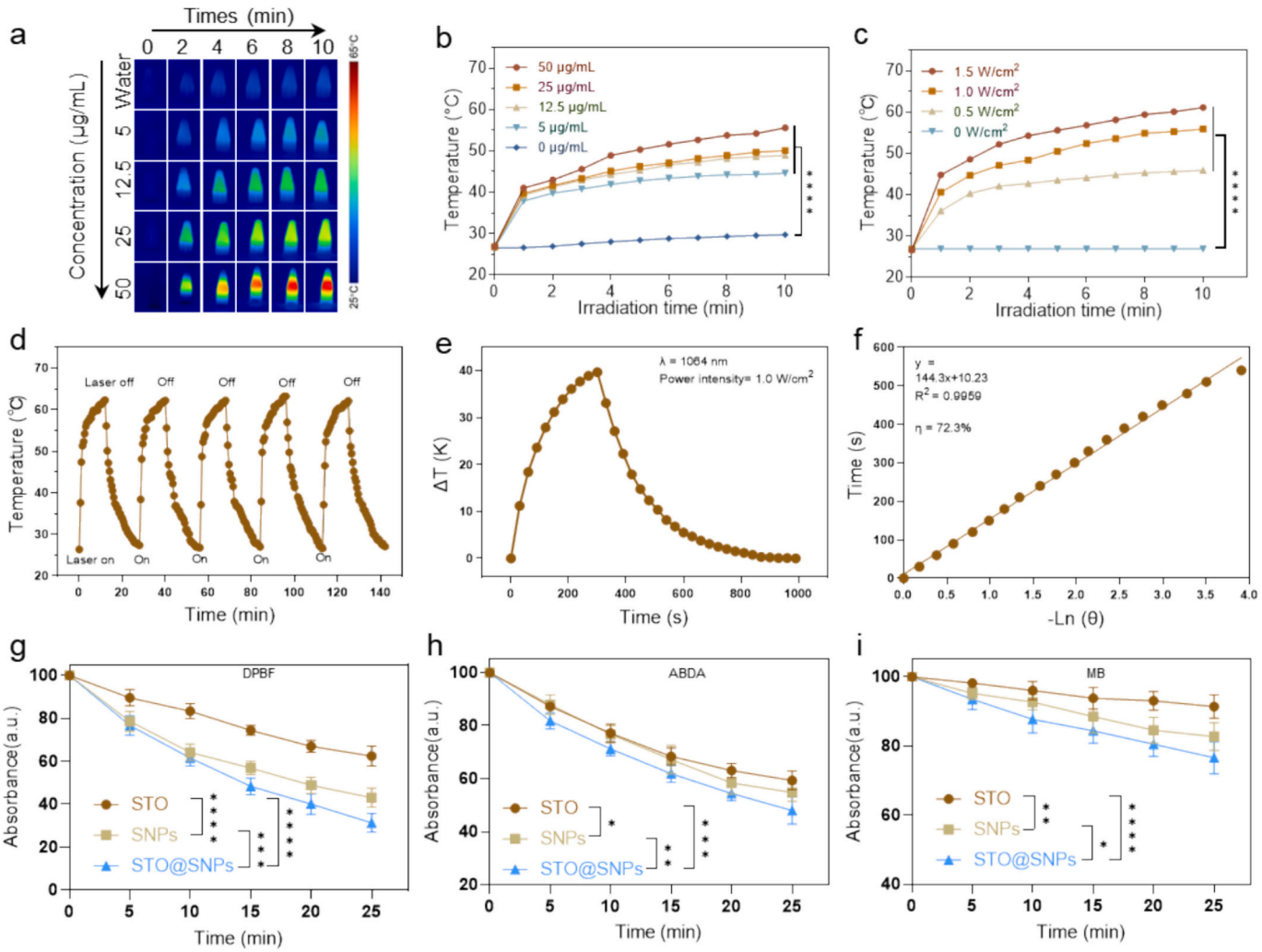

Fig. 3. Light-heat-electrochemical catalytic performance. (a) Infrared thermal imaging of SNPs solutions at different concentrations under 1064 nm laser irradiation at 1.0 W cm^{-2}. (b) Temperature changes of SNPs solutions at different concentrations under 1064 nm laser irradiation at 1.0 W cm^{-2}. (c) temperature changes of SNPs solutions under different laser powers at the same concentration. d) Five cycles of heating and cooling curves of SNPs solutions with the 1064 nm laser on-off. e) Heating and cooling curves of SNPs solutions under 1064 nm laser irradiation. f) Linear relationship between the cooling time and -lnθ with a calculated photothermal conversion efficiency (η) of 72.3%. (g) Variation of the DPBF absorption peak at 420 nm for STO, SNPs, and STO@SNPs (75 μg/mL) under 1064 nm laser irradiation at 1.5 W/cm^2, reflecting $\cdot O_2^-$ generation. (h) Variation of the ABDA absorption peak at 400 nm for STO, SNPs, and STO@SNPs (50 μg/mL) under 1064 nm laser irradiation at 1.5 W/cm^2, reflecting $^1O_2$ generation. (i) Variation of the MB absorption peak at 680 nm for STO, SNPs, and STO@SNPs (50 μg/mL) under 1064 nm laser irradiation at 1.5 W/cm^2, reflecting·OH generation.

52% at the same concentration, showing an approximately 7% improvement compared with SNPs alone, with a similar dependence on laser power (Fig. 3h, Fig. S7). These results demonstrate that STO@SNPs efficiently generate ROS under 1064 nm irradiation, and the photothermal-thermoelectric cascade energy conversion significantly enhances the NIR-II photodynamic therapy performance compared with single SNPs. Then, the ability of the STO, SNPs and STO@SNPs to catalyze the generation of ·OH was investigated, using methylene blue (MB) as the detector. Fig. 3i and Fig. S8 shows that within a 25-min light exposure period, the MB content in both STO, SNPs and STO@SNPs group decreased to 92.4%, 83.2%, and 76.4%, respectively. The probe used for ROS detection may experience photodegradation and non-specific degradation. To more accurately identify the types of ROS catalyzed by STO@SNPs, electron spin resonance (ESR) spectroscopy was employed. This method allowed for the detection of $\cdot O_2^-$, $^1O_2$, and ·OH using 2,2,6,6-tetramethylpiperidine (TEMP) and 5,5-dimethyl-1-pyrroline N-oxide (DMPO) as spin trapping agents. As exhibited in Fig. S9, both $\cdot O_2^-$, $^1O_2$, and ·OH signals were detected in the system for the STO@SNPs after laser radiation.

To further clarify the ROS-generating behavior of the STO thermoelectric material under temperature variation, DPBF was used as an indicator. Briefly, 50 μg/mL STO was mixed with the DPBF probe, and the UV–vis absorption spectrum was first measured at 25 °C. The mixed solution was then placed in water baths at 25 °C, 27.5 °C, 30 °C and 35 °C for 3 min, followed by a second UV–vis measurement. The results showed that STO could already be activated to generate ROS under a temperature difference of 2.5 °C, indicating its excellent thermal-triggered catalytic activity (Fig. S10). To evaluate the thermoelectric activation behavior of STO, the current–time response under temperature variation was measured using an electrochemical workstation in a standard three-electrode system. As shown in Fig. S11, STO exhibited a clear and rapidly increased current signal under temperature-variation conditions, whereas only a negligible current response was observed in the absence of temperature change. The current gradually rose and reached a stable plateau after thermal stimulation, indicating that STO could efficiently convert thermal fluctuation into an electrical response. These results demonstrate that STO possesses excellent heat-responsive electrical properties, which provide direct evidence for its

thermoelectric activation behavior and further support its role in the light-heat-electric cascade process.

3.3. In vitro biocompatibility and antitumor activity

The in vitro antitumor potential of STO@SNPs nanoparticles was first assessed by evaluating their biocompatibility and baseline cytotoxicity, which is essential to ensure their safety for biomedical applications. Two cell lines, normal colon epithelial cells (NCM460) and colon cancer cells (CT26), were employed. CCK-8 assays showed that cell viability remained above 90% for both cell lines even at a high concentration of 100 μg/mL (Fig. 4a, b), confirming the excellent biocompatibility of the nanoparticles. To investigate the therapeutic potential, CT26 cells were then treated with varying concentrations of STO, SNPs, and STO@SNPs under 1064 nm laser irradiation (1.0 W cm^{-2}, 5 min per well). Cell viability decreased in a concentration-dependent manner, with STO@SNPs reducing viability to less than 10% at the highest concentration, indicating that, although intrinsically nontoxic, these nanoparticles effectively induced cancer cell death upon NIR-II irradiation (Fig. 4c). In the STO group, cell viability showed a moderate reduction, dropping to 72%. Based on previous experimental results, this reduction in viability may be attributed to the slight temperature increase in the solution caused by laser irradiation, which activates the catalytic activity of the STO. In the SNPs group, a significant decrease in cell viability was observed, with viability reaching 29%, suggesting photoactivation upon laser exposure. Notably, although SNPs significantly affected cell viability under laser irradiation, their effect is still considerably less efficient at inducing cell death compared to STO@SNPs. This suggests that the heat generated by SNPs under laser irradiation effectively activates STO, enhancing its therapeutic potential.

Given that ROS generation is a key mechanism underlying catalytic therapy, intracellular ROS production was evaluated using DCFH-DA as a fluorescent probe. Confocal microscopy revealed strong green fluorescence in SNPs + L and STO@SNPs + L treated cells, indicating substantial ROS production (Fig. 4d). To quantitatively validate these observations, flow cytometry was performed, which confirmed significantly higher ROS levels in the SNPs + L and STO@SNPs + L groups compared to controls (Fig. 4e). These results establish that STO@SNPs nanoparticles efficiently generate ROS under NIR-II irradiation, providing a mechanistic basis for their photodynamic cytotoxicity. Finally, to directly assess the functional consequences of ROS generation and photothermal effects, cell viability and apoptosis were evaluated using live/dead staining (Calcein AM/PI) and Annexin V-FITC assays. Consistently, these analyses revealed extensive cell death in SNPs + L and STO@SNPs + L groups, with late apoptosis rates reaching 55.69% and 58.63%, respectively (Fig. 4f, g). Together, these results demonstrate that STO@SNPs nanoparticles combine low inherent cytotoxicity with strong NIR-II-triggered photothermal and photodynamic effects, effectively inducing cancer cell death, and highlight their considerable potential as a photothermal–photodynamic–thermoelectric cascade energy conversion catalytic therapeutic strategy.

γ-H2AX is used as a marker to assess DNA damage in CT26 cells induced by STO, SNPs, and STO@SNPs under 1064-nm laser irradiation. Confocal laser scanning microscopy images (Fig. 4h) show that no obvious green fluorescence was detected in control group, L group, STO@SNPs group, while there was weak green fluorescence on the cell nucleus surface in STO + L group. In contrast, in the SNPs + L, and STO@SNPs + L groups, there was a large amount of green fluorescence on the cell nucleus surface. Quantitative analysis of the green fluorescence intensity further confirmed these results (Fig. S12), indicating that STO@SNPs can effectively induce DNA damage under laser irradiation.

Immunofluorescence staining showed that compared with the Control, L, and STO@SNPs groups, HSP70 expression was markedly elevated in the laser-treated groups, with the strongest fluorescence intensity observed in the STO@SNPs + L and SNPs + L groups (Fig. S13). These results indicate that the heat-generating treatment effectively induces HSP70 upregulation, suggesting activation of cellular heat-stress responses and a potential contribution to subsequent antitumor immune regulation.

The penetration of the drug into the deep layer of the tumor is the key factor for the efficacy of the drug. The ability of STO@SNPs to penetrate tumors was evaluated using 3D spheroids of CT26 cells. The penetration of STO@SNPs into the spheroids was compared with that of the control group. The results presented in Fig. S14 demonstrate that STO@SNPs exhibited significantly superior permeability within the tumor spheroids compared to the control. This enhanced permeability is attributed to the presence of the folate (FA) molecule on the surface of STO@SNPs, which facilitates the targeted delivery of therapeutic agents deeper into the tumor core.

3.4. In vitro evaluation of DC maturation and T cell activation

Beyond direct cytotoxicity, phototherapy can induce immunogenic cell death (ICD), a process in which dying tumor cells release damage-associated molecular patterns (DAMPs) and tumor-associated antigens (TAAs). Among these, calreticulin (CRT) translocation from the endoplasmic reticulum to the cell membrane serves as a hallmark of ICD, enhancing antigen presentation and activating tumor-specific immune responses. CLSM analysis revealed markedly higher CRT expression in SNPs+L and STO@SNPs + L groups compared with other treatments (red fluorescence, Fig. 5a), indicating that STO@SNPs nanoparticles effectively trigger ICD through synergistic photothermal, photodynamic, and thermoelectric effects. Furthermore, in these groups, the expression of HMGB1 on the nuclear surface was significantly reduced (Fig. 5b). These results indicate that the nanoparticles based on STO@SNPs, when excited by a 1064-nm laser, enhance oxidative stress by catalyzing the production of ROS and effectively induce the ICD of tumor cells.

ICD further promoted dendritic cell (DC) maturation and antigen presentation. CT26 cells from different treatment groups were co-cultured with bone marrow-derived dendritic cells (BMDCs) in a transwell system for 24 h. Flow cytometry analysis showed that DC maturation ($CD11c^+CD80^+CD86^+$) was significantly enhanced in STO + L, SNPs + L and STO@SNPs + L groups, reaching 24.4%, 28.9% and 31.4%, respectively, compared with 14.6% in the control group (Fig. 5c-e). Dendritic cells (DCs) play a central role in antitumor immunity as primary antigen-presenting cells (APCs), capable of recognizing, capturing, and processing tumor antigens, which are then presented to T cells to initiate specific antitumor immune responses. Induction of ICD in tumor cells can further enhance DC maturation and antigen-presenting capacity, promoting T cell proliferation and activation, particularly $CD8^+$ cytotoxic T lymphocytes. The subsequent activation of T cells was then assessed. $CD4^+$ T cell activation reached 38.4%, 39.7% and 58.4% in the STO + L, SNPs + L and STO@SNPs + L groups, respectively, compared with 33.1% in the control group (Fig. 5f, g). $CD8^+$ T cell activation was 16.1% in STO + L group, 25.9% in the SNPs+L group and increased to 34.5% in the SNPs + L group, over three times higher than the control group (10.6%) (Fig. 5h, i). These results demonstrate that under 1064 nm laser irradiation, STO@SNPs nanoparticles not only enhance DC maturation and upregulate co-stimulatory molecules (CD80/CD86), but also effectively activate both $CD4^+$ and $CD8^+$ cytotoxic T cells, thereby significantly amplifying antitumor immune responses.

3.5. Evaluation of antitumor effects in vivo

STO@SNPs nanoparticles exhibit thermal-to-light conversion, photothermal catalysis, and thermoelectric catalysis performance under 1064 nm laser irradiation. Their tumor-targeting capability via the FA, EPR effect enables preferential accumulation in tumor tissues, thereby enhancing therapeutic efficacy while minimizing systemic toxicity. The

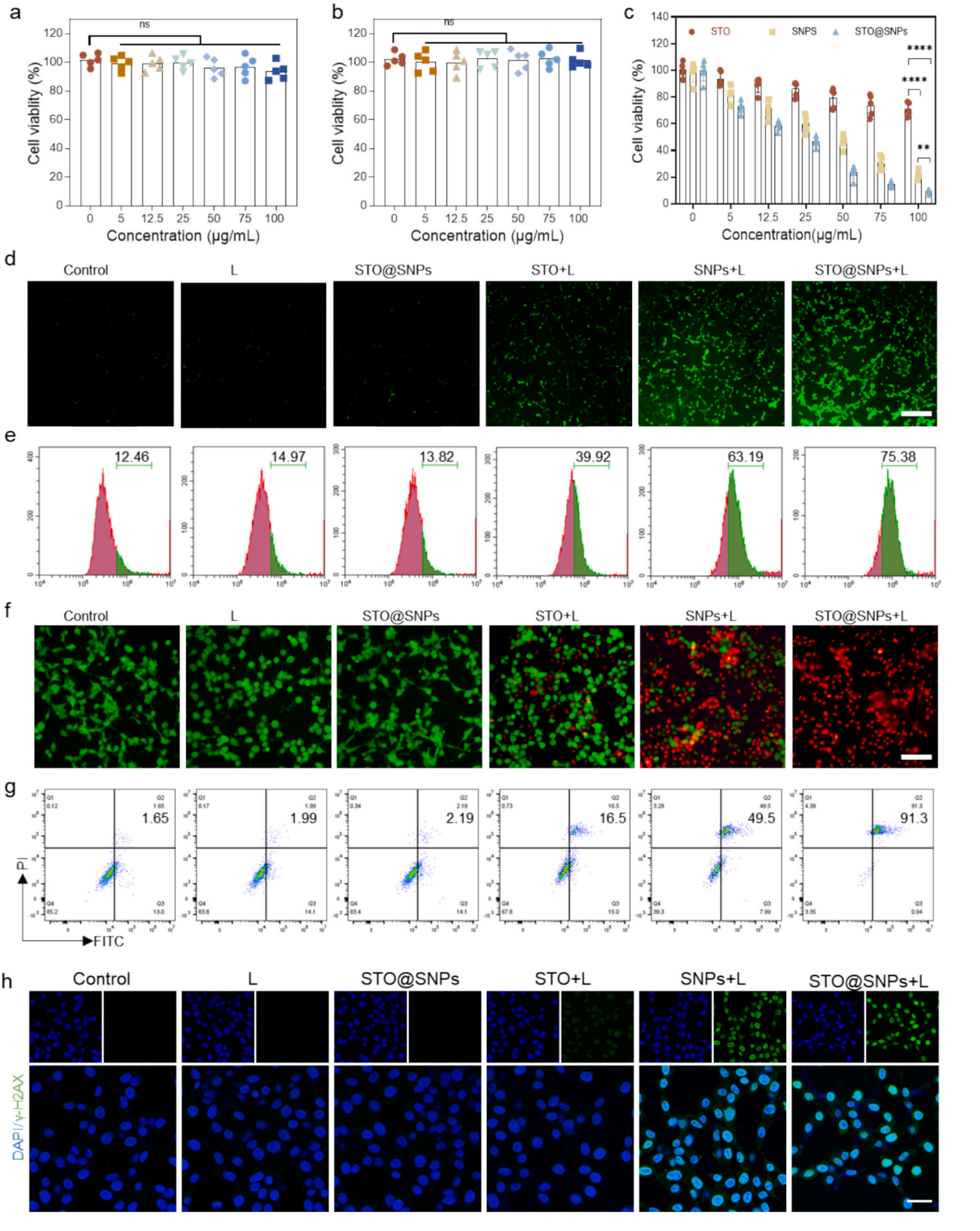

(caption on next page)

Fig. 4. In vitro cytotoxicity and tumor cell killing evaluation of STO, SNPs, and STO@SNPs. This figure illustrates the impact of different treatments on cell viability, ROS production, and apoptosis in cancer and normal cells. (a) Dose-dependent effects of skop on CT26 cell viability ($n = 5$). (b) Dose-dependent effects of skop on NCM460 cell viability (n = 5). (c) Effects of 1064 nm laser irradiation with intensity of 1.0 W/cm^2 combined with STO, SNPs, and STO@SNPs at different concentrations on CT26 cell viability (n = 5). (d) Fluorescence microscopy images showing ROS generation in CT26 cells under various treatments. Scale bar = 400 μm. The concentration of STO, SNPs, and STO@SNPs was 50 μg/mL. For light-treated groups, cells were irradiated with a 1064 nm laser at 1.0 W/cm^2 for 5 min. (e) Flow cytometry analysis of ROS generation in treated CT26 cells with the same treatment in (d). (f) Merged fluorescence microscopy images of live/dead cell staining in different treatment groups. Scale bar = 200 μm. The concentration of STO, SNPs, and STO@SNPs was 100 μg/mL. For light-treated groups, cells were irradiated with a 1064 nm laser at 1.0 W/cm^2 for 5 min. (g) Flow cytometry analysis of apoptosis in treated CT26 cells with the same treatment in (f). (h) CLSM images showing DNA damage in CT26 cells marked by γ-H2AX under different treatments; Scale bar = 50 μm. The concentration of STO, SNPs, and STO@SNPs was 50 μg/mL. For light-treated groups, cells were irradiated with a 1064 nm laser at 1.0 W/cm^2 for 5 min.

metabolism and release of STO@SNPs in a mouse model of colorectal cancer were first evaluated using fluorescent dyes. Small animal fluorescence imaging technology was employed to monitor the biodistribution of the injected drug in real time. One hour after injection, a distinct fluorescence signal was observed in the liver of the mice, suggesting that the drug underwent hepatic metabolism. Subsequently, the fluorescence intensity in the intestinal tumor area gradually increased. Eight hours post-injection, the fluorescence signal in the tumor reached its peak, indicating effective delivery and retention of the drug in the tumor tissue. These results highlight the excellent targeting ability of STO@SNPs toward tumor tissue. After 24 h, the fluorescence signal in the tumor significantly diminished, suggesting that the drug had been metabolized and cleared from the body. This time-dependent metabolism further underscores the favorable safety profile of the drug (Fig. 6a, b).

Plasma pharmacokinetics of STO@SNPs after intravenous administration was evaluated by ICP-MS. After intravenous injection, the plasma concentration of STO@SNPs exhibited a rapid initial decline followed by a relatively slow elimination phase (Fig. S15). These results indicate that STO@SNPs were quickly distributed from the bloodstream into tissues and organs after administration, and then underwent gradual systemic clearance rather than immediate complete removal. Such pharmacokinetic behavior suggests that the nanoplatform retained a certain circulation time in vivo, which is favorable for continuous transport to the tumor site. Combined with the in vivo fluorescence imaging results showing that the tumor signal reached a high level at 8 h post-injection, it can be inferred that the blood circulation and tumor accumulation processes of STO@SNPs were well matched temporally.

The orthotopic colorectal tumors established in this study were located in the cecum. In mice, the cecum is positioned on the right side of the abdominal cavity in a relatively fixed anatomical location and lies close to the abdominal wall. Measurements indicated that the combined thickness of the overlying abdominal skin and peritoneum above the cecum was approximately 1 mm (Fig. S16), which is substantially smaller than the reported penetration depth of NIR-II light (>1 cm). [42] Therefore, 1064 nm laser irradiation is sufficient to penetrate the overlying tissues and effectively activate STO@SNPs for the treatment of orthotopic colorectal tumors in mice.

To evaluate their antitumor performance, an orthotopic colorectal cancer model was established, and tumor progression was longitudinally monitored using IVIS imaging. Mice were randomly assigned to six groups (Control, L, STO@SNPs, STO + L, SNPs + L, and STO@SNPs + L) and treated via intravenous injection on Day 1 and Day 3. Eight hours post-injection, tumors were irradiated with a 1064 nm laser (0.7 W cm^{-2}, 8 min) (Fig. 6c). Infrared thermal imaging revealed a significant temperature increase in the tumor regions of the STO@SNPs+L group, reaching 52 °C (Fig. S17). By Day 9, IVIS imaging and tissue dissection revealed significant differences among treatment groups (Fig. 6d-f). In the SNPs + L group, four of five mice showed marked tumor regression, with one mouse achieving complete tumor eradication. Remarkably, STO@SNPs+L treatment resulted in near-complete tumor elimination in all mice, highlighting the synergistic effect of the STO@SNPs design. In contrast, STO + L and SNPs alone produced limited tumor inhibition, demonstrating that neither component alone is sufficient to achieve maximal therapeutic outcomes under laser irradiation. Importantly, no significant body weight changes were observed in any group, indicating favorable systemic biocompatibility (Fig. 6g).

Histological analysis further confirmed these findings. H&E staining revealed extensive tumor necrosis in the SNPs + L and STO@SNPs + L groups, characterized by nuclear condensation, cell lysis, and reduced cellular density (Fig. 6h). TUNEL assays confirmed widespread apoptosis within these tumor regions, consistent with the enhanced ROS generation and local hyperthermia induced by laser-activated STO@SNPs nanoparticles (Fig. 6i). The superior antitumor efficacy of STO@SNPs can be attributed to the cascade photothermal-thermoelectric energy conversion, which not only elevates tumor temperature to cytotoxic levels but also generates ROS through thermoelectric catalysis, collectively inducing apoptosis more efficiently than either component alone. Overall, these results demonstrate that STO@SNPs heterogeneous junction nanoparticles integrate multiple therapeutic modalities-photothermal, photocatalytic, and thermoelectrocatalytic effects-into a single platform. Their tumor-targeting capability, combined with synergistic energy conversion under NIR-II irradiation, enables effective tumor ablation while maintaining overall safety, highlighting strong potential for colon cancer treatment.

3.6. Enhanced immune response in vivo

Under 1064 nm irradiation, STO@SNPs nanoparticles generated a rapid burst of ROS, triggering ICD and the release of abundant tumor-associated antigens. To delineate the resulting immune cascade and its impact on the tumor immune microenvironment, we systematically analyzed DCs and T cells within the tumor, draining lymph nodes, and spleen (Fig. 7a).

Within the tumor, flow cytometry revealed a marked elevation in the population of mature DCs expressing co-stimulatory molecules CD80 and CD86. The proportion of mature DCs (CD80$^+$CD86$^+$) reached 34.7% in the STO@SNPs + L group, compared to 26.2% in the SNPs + L group and only 7.86% in controls (Fig. 7b). This pronounced DC maturation suggests that the STO@SNPs-induced oxidative stress effectively promotes antigen capture and presentation, initiating a potent local immune activation. We next evaluated DC migration to secondary lymphoid organs. A significant increase in mature CD80$^+$CD86$^+$ DCs was detected in the draining lymph nodes of the STO@SNPs + L group, reaching 32.1%, the highest among all groups (Fig. 7c). This enhancement indicates that the photoactivated STO@SNPs system not only stimulates intratumoral antigen-presenting cells but also facilitates their trafficking to lymphoid tissues, thereby amplifying T-cell priming and immune propagation.

Concomitantly, STO@SNPs+L treatment induced a pronounced infiltration of effector T cells into the tumor microenvironment. The proportions of CD4$^+$ helper T cells and CD8$^+$ cytotoxic T lymphocytes (CTLs) were significantly increased to 37.25% and 33.63%, respectively, in the STO@SNPs+L group, compared with only 9.57% and 15.5% in the control group (Fig. 7d, e). This marked enrichment of tumor-infiltrating T cells indicates that the treatment effectively enhances tumor antigen presentation and promotes strong cellular immune activation. Considering our previous findings that STO@SNPs+L induced ICD-related signals, including CRT exposure, HMGB1 release, and HSP70 upregulation, these results further suggest that the therapy

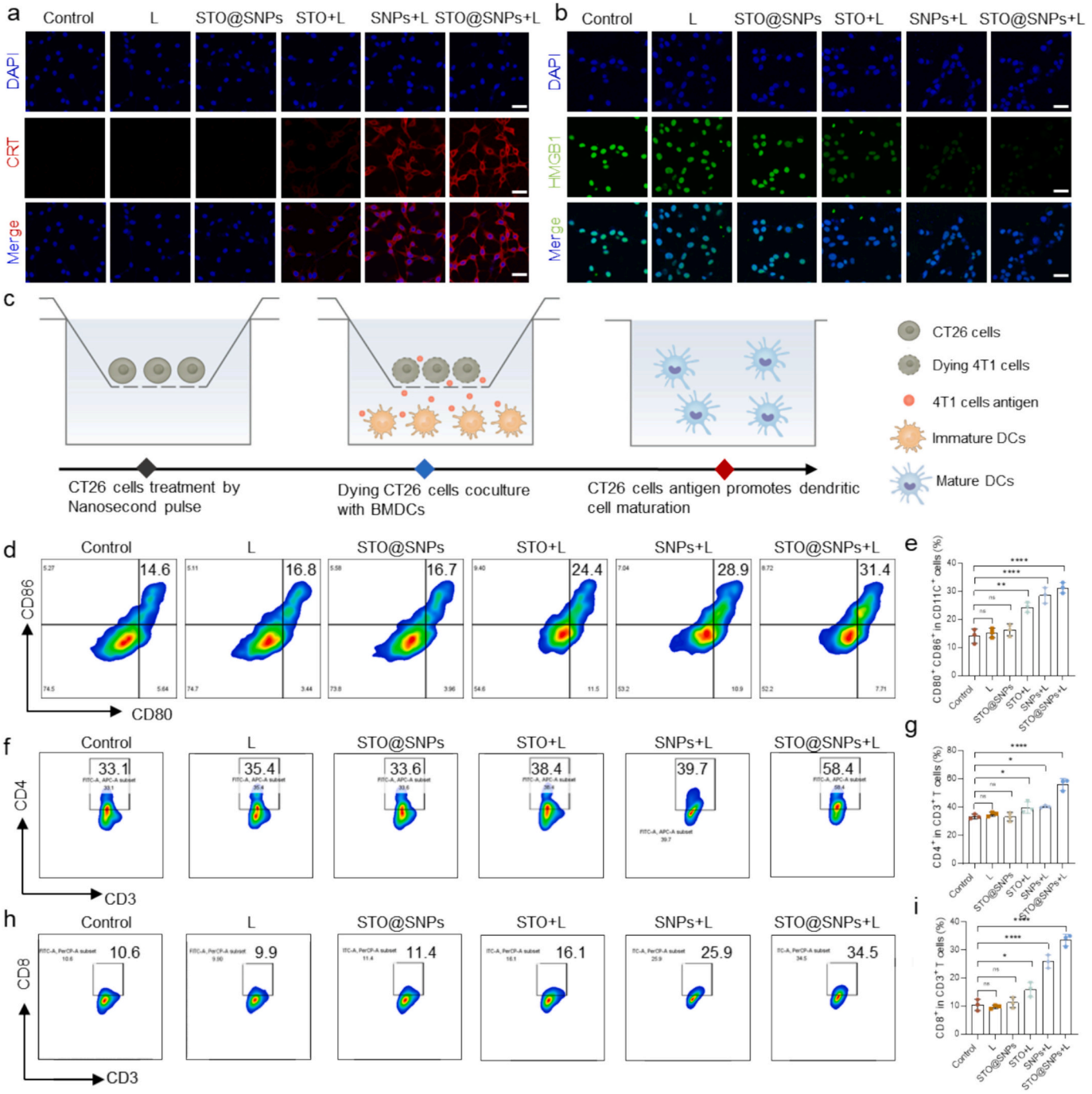

Fig. 5. In vitro evaluation immunogenic cell death, and immune cell activation. (a) Representative CLSM images showing CRT exposure in cells after various treatments. Scale bar = 50 μm. The concentration of STO, SNPs, and STO@SNPs was 50 μg/mL. For light-treated groups, cells were irradiated with a 1064 nm laser at 1.0 W/cm^2 for 5 min. (b) Representative CLSM images showing HMGB1 exposure in cells after various treatments. Scale bar = 50 μm. The concentration of STO, SNPs, and STO@SNPs was 50 μg/mL. For light-treated groups, cells were irradiated with a 1064 nm laser at 1.0 W/cm^2 for 5 min. (c) Schematic diagram of experimental design for in vitro CT26 cancer cell and BMDC co-culture assay using a transwell system. (d) FCM analysis of DC maturation under different treatment conditions. The concentration of STO, SNPs, and STO@SNPs was 50 μg/mL. For light-treated groups, cells were irradiated with a 1064 nm laser at 1.0 W/cm^2 for 5 min. (e) Quantification of DC maturation from (d). (f) FCM analysis of CD4$^+$ T cells after various treatments. The concentration of STO, SNPs, and STO@SNPs was 50 μg/mL. For light-treated groups, cells were irradiated with a 1064 nm laser at 1.0 W/cm^2 for 5 min. (g) Quantification of CD4$^+$ T cell data from (f). (h) FCM analysis of CD8$^+$ T cells after different treatments. The concentration of STO, SNPs, and STO@SNPs was 50 μg/mL. For light-treated groups, cells were irradiated with a 1064 nm laser at 1.0 W/cm^2 for 5 min. (i) Quantification of CD8$^+$ T cell data from (h).

facilitates the release and presentation of tumor-associated antigens, thereby creating favorable conditions for adaptive immune priming. To further verify whether the increased intratumoral T-cell infiltration was accompanied by functional immune activation, we additionally performed flow cytometric analysis of intratumoral cytokines. As shown in Fig. S18, the STO@SNPs + L group exhibited a significantly higher proportion of cytokine-positive immune cells in tumor tissues than the control groups, indicating that the infiltrating immune cells were not only increased in number, but were also functionally activated. Combined with the enhanced dendritic cell maturation observed in both

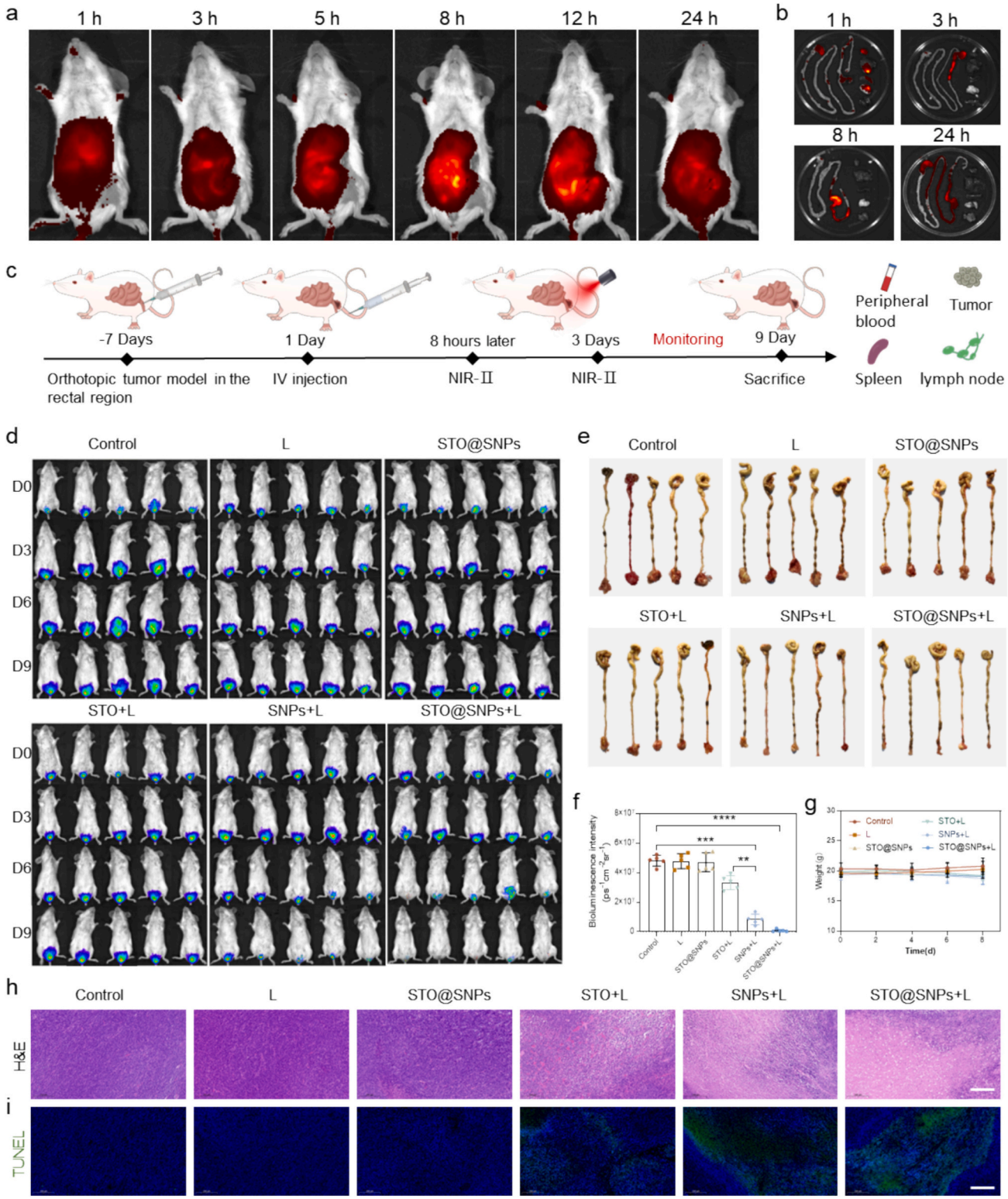

Fig. 6. In vivo evaluation of antitumor effects. (a) In vivo optical live imaging was conducted on orthotopic CRC mice at different time points after tail vein injection of ICG-labeled STO@SNPs. (b) Fluorescence images of major organs from mice at different time points. (c) Schematic illustration of the in vivo antitumor therapy protocol. All treatment groups received intravenous injections (200 μL total volume) of STO, SNPs, or STO@SNPs at a dose of 5 mg/kg. Mice in the laser-treated groups were irradiated at the tumor site with a 1064 nm laser (0.7 W/cm^2) for 8 min. (d) Representative images of orthotopic ovarian cancer-bearing mice from different treatment groups. (e) Representative images of orthotopic ovarian tumors excised from mice in different treatment groups. (f) Quantitative analysis of fluorescence signals in the tumor regions from small animal images at the end of treatment (n = 5). (g) Body weight curves of mice during the treatment period. (h) Representative hematoxylin and eosin (H&E) staining images of tumor sections from different treatment groups. Scale bar = 200 μm. (i) Representative TUNEL staining images of tumor sections from different treatment groups, indicating apoptotic cells. Scale bar = 200 μm.

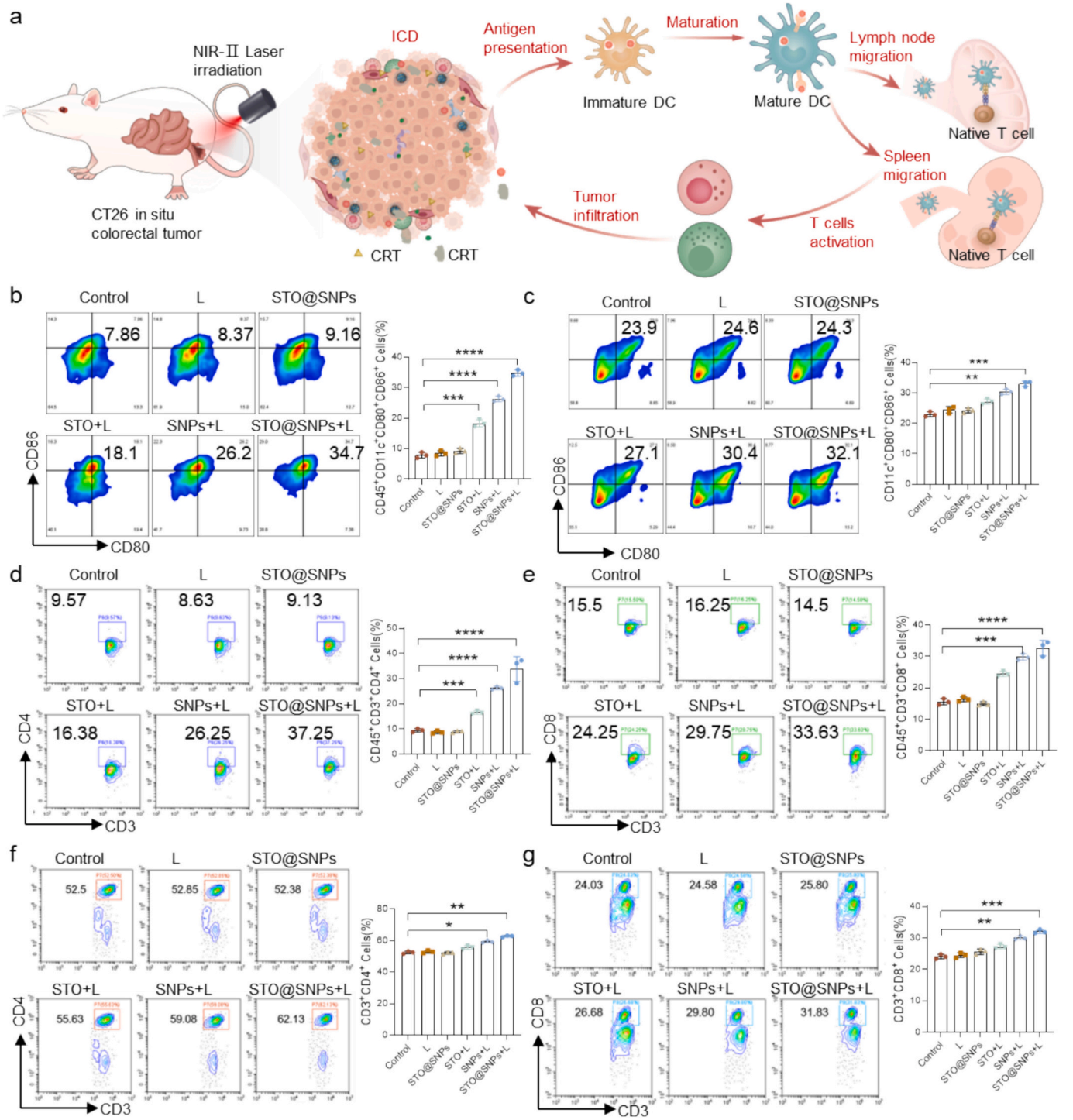

Fig. 7. In vivo analysis of immunological responses. (a) Schematic diagram of immune activation principle. (b) FCM analysis of intratumoral DC maturation, with corresponding quantitative data. (c) FCM analysis of DC maturation in lymphatic tissues, with corresponding quantitative data. (d) FCM analysis of intratumoral $CD4^+$ T cells, with corresponding quantitative data. (e) FCM analysis of intratumoral $CD8^+$ T cells, with corresponding quantitative data. (f) FCM analysis of $CD4^+$ T cells in spleen tissue, with corresponding quantitative data. (g) FCM analysis of $CD8^+$ T cells in spleen tissue, with corresponding quantitative data.

tumor tissues and draining lymph nodes, these findings demonstrate that STO@SNPs + L not only triggers ICD-mediated antigen release, but also promotes antigen processing and presentation, T-cell recruitment, and cytokine-associated effector activation within the tumor microenvironment. Therefore, the treatment establishes a more immunostimulatory and functionally active antitumor immune microenvironment, which collectively contributes to its potent therapeutic efficacy.

Given that the spleen is a major peripheral immune organ involved in T-cell expansion, activation, and immune memory formation, we further analyzed splenic lymphocyte populations to evaluate whether the local therapeutic effect of STO@SNPs + L could translate into systemic antitumor immune activation. As shown in Fig. 7f, g, the percentages of both $CD8^+$ T cells and $CD4^+$ T cells in the spleen were markedly increased in the STO@SNPs + L group, reaching 31.83% and 62.13%, respectively, compared with 24.03% and 52.5% in the control group. These results indicate that the STO@SNPs-mediated treatment not only exerts local

tumoricidal effects, but also activates a broader systemic immune response. In particular, the expansion of $CD4^+$ T cells is of special importance, as these cells can provide helper signals for antigen presentation and immune amplification, promote the activation and proliferation of $CD8^+$ cytotoxic T cells, and support the establishment of long-term immune surveillance. To further determine whether this systemic immune activation could be translated into durable antitumor immunity, we additionally performed flow cytometric analysis of memory T-cell populations in the spleen. As shown in Fig. S19, the STO@SNPs + L group exhibited significantly increased proportions of both $CD4^+$ memory T cells and $CD8^+$ memory T cells compared with the control groups. The elevation of these memory T-cell subsets suggests that the treatment not only triggers an acute immune response against tumors, but also facilitates the generation of long-term immunological memory. Combined with the observed enhancement of splenic $CD4^+$ and $CD8^+$ T-cell populations, these findings demonstrate that STO@SNPs + L can induce robust systemic adaptive immune activation beyond the local tumor site and promote the formation of lasting antitumor immune memory. Such immune remodeling is highly beneficial for maintaining sustained immune surveillance, thereby contributing to the overall antitumor immunotherapeutic efficacy and potentially reducing tumor recurrence and metastasis.

These findings demonstrate that STO@SNPs nanoparticles under NIR-II irradiation orchestrate a multilevel immune activation through photothermal-thermoelectric synergistic energy conversion. The treatment induces ROS-mediated ICD, drives DC maturation and migration, and activates both intratumoral and systemic T-cell responses. This coordinated immune modulation confers a potent and durable antitumor effect, underscoring the promise of STO@SNPs-based photo-thermoelectric nanoplatforms for the immunotherapeutic management of colorectal cancer.

3.7. In vivo biological safety analysis

In this study, we performed a comprehensive in vivo safety evaluation of STO@SNPs, with a focus on hematological parameters and histopathological changes in major organs. Hematoxylin-eosin (HE) stained sections of the heart, liver, spleen, lung, and kidney exhibited intact tissue architecture, well-organized cellular arrangement, and no evidence of increased inflammatory responses or tissue injury compared with the control group. Detailed pathological examination revealed no significant abnormalities, including necrosis, hemorrhage, infarction, or fibrosis, in any of the examined organs (Fig. S20). The comprehensive analysis of hematological and biochemical parameters in mice demonstrated no significant differences between the treatment and control groups across key indicators, including white blood cell count, hemoglobin levels, platelet count, as well as markers of liver and kidney function. All measured values remained within established normal reference ranges (Fig. S21, S22). These results suggest that, under the administered dosage and treatment regimen, the compound does not elicit appreciable systemic toxicity. The absence of hematological or biochemical abnormalities further supports the favorable safety profile of the treatment, indicating its suitability for continued preclinical evaluation and potential translational applications.

4. Conclusion

In this study, the STO@SNPs nanoparticles demonstrated the synergistic advantages of NIR-II-triggered photothermal, photodynamic, and thermoelectric cascade energy conversion. The unique acceptor–donor–acceptor (A-D-A) molecular structure of SKCN significantly enhances ICT, which improves light absorption and photothermal conversion efficiency within the NIR-II window, rendering it suitable for deep-seated tumor therapy. The formation of STO@SNPs with the thermoelectric material STO, combined with PEGylation, not only enhanced aqueous stability and prolonged systemic circulation but also facilitated tumor-targeted accumulation via the EPR effect, providing an effective platform for localized tumor therapy.

Under 1064 nm laser irradiation, STO@SNPs nanoparticles simultaneously photothermal, photocatalytic, and thermoelectric catalytic effects, inducing efficient tumor cell apoptosis and exhibiting pronounced in vitro antitumor activity. Notably, ROS-mediated cellular stress and cell death-initiated ICD, promoting CRT exposure and the release of damage-associated molecular patterns (DAMPs). This, in turn, enhanced DC maturation and antigen presentation. In vivo, STO@SNPs treatment significantly increased DC maturation within tumors, elevated $CD4^+$ and $CD8^+$ T cell populations, and triggered systemic immune activation in both lymph nodes and spleen, indicating that the nanoparticles not only ablate primary tumors locally but also potentiate systemic antitumor immunity, potentially preventing recurrence and metastasis. Further in vivo studies confirmed that STO@SNPs effectively inhibited tumor growth and, in some cases, achieved complete tumor regression in an orthotopic colorectal cancer model, without observable toxicity or tissue damage in major organs, demonstrating favorable biosafety. This highlights the dual advantage of deep tumor-targeted therapy and systemic safety, establishing a solid foundation for potential clinical translation.

The innovation of this work lies in the integration of photothermal, photocatalytic, and thermoelectric catalytic modalities within a single nanoparticle platform, enabling efficient energy conversion in deep tissues while concurrently activating antitumor immunity. This strategy overcomes the limitations of conventional monomodal phototherapy regarding tissue penetration and immune stimulation, providing a multifunctional nanoplatform capable of tumor-targeted therapy. Future investigations could further optimize nanoparticle biodegradability and immunomodulatory capacity, and potentially combine this approach with immune checkpoint inhibitors to achieve more robust and durable antitumor responses. Overall, STO@SNPs nanoparticles exhibit exceptional cascade energy conversion efficiency, potent immunostimulatory effects, and favorable biocompatibility, underscoring their promise as a multimodal photothermal–photodynamic–thermoelectric therapy strategy for deep-seated tumors.

In addition, for colorectal tumors located in the distal bowel and accessible through the anus, direct endoluminal light delivery represents a highly promising strategy. In such cases, insertion of an optical fiber via the anal route could substantially shorten the light propagation path, reduce attenuation caused by overlying tissues, and enable more precise and localized irradiation of the tumor lesion. This approach may enhance therapeutic efficiency while minimizing off-target exposure to surrounding normal tissues. In future investigations, we plan to systematically evaluate fiber-assisted intraluminal laser delivery, to further improve translational feasibility and therapeutic performance in orthotopic colorectal cancer models.

CRediT authorship contribution statement

Baoli Zhou: Formal analysis, Data curation. **Ruiyan Li:** Methodology, Data curation. **Guangkun Song:** Methodology, Data curation. **Gaoli Niu:** Software, Data curation. **Jingwen Han:** Writing – review & editing. **Yongsheng Chen:** Supervision, Resources. **Lingling Xu:** Project administration, Formal analysis. **Xiaoyuan Ji:** Supervision, Project administration, Funding acquisition, Conceptualization. **Yong Kang:** Supervision, Resources, Project administration, Conceptualization.

Declaration of competing interest

The authors declare that they have no known competing financial interests or personal relationships that could have appeared to influence the work reported in this paper.

Acknowledgements

This study was financially supported by grants from the National Natural Science Foundation of China (Grant No. 32501189), Beijing-Tianjin-Hebei Natural Science Foundation Cooperation Project (Grant No. 25JJJJC0017).

Appendix A. Supplementary data

Supplementary data to this article can be found online at https://doi.org/10.1016/j.cej.2026.175390.

Data availability

Data will be made available on request.

References

[1] Q. Pan, X. Fan, L. Xie, D. Wu, R. Liu, W. Gao, K. Luo, B. He, Y. Pu, Nano-enabled colorectal cancer therapy, J. Control. Release 362 (2023) 548–564, https://doi.org/10.1016/j.jconrel.2023.09.014.
[2] K. Ying, B. Bai, X. Gao, Y. Xu, H. Wang, B. Xie, Orally administrable therapeutic nanoparticles for the treatment of colorectal cancer, Front. Bioeng. Biotechnol. (2021), https://doi.org/10.3389/fbioe.2021.670124. Volume 9–2021.
[3] C. Eng, T. Yoshino, E. Ruíz-García, N. Mostafa, C.G. Cann, B. O'Brian, A. Benny, R. O. Perez, C. Cremolini, Colorectal cancer, Lancet 404 (10449) (2024) 294–310, https://doi.org/10.1016/s0140-6736(24)00360-x.
[4] K.W. Davidson, M.J. Barry, C.M. Mangione, M. Cabana, A.B. Caughey, E.M. Davis, K.E. Donahue, C.A. Doubeni, A.H. Krist, M. Kubik, L. Li, G. Ogedegbe, D.K. Owens, L. Pbert, M. Silverstein, J. Stevermer, C.W. Tseng, J.B. Wong, U.S.P. Servi, Screening for colorectal cancer: US preventive services task force recommendation statement, Jama-J. Am. Med. Assoc. 325 (19) (2021) 1965–1977, https://doi.org/10.1001/jama.2021.6238.
[5] S.G. Patel, J.J. Karlitz, T. Yen, C.H. Lieu, C.R. Boland, The rising tide of early-onset colorectal cancer: a comprehensive review of epidemiology, clinical features, biology, risk factors, prevention, and early detection, Lancet Gastroenterol. 7 (3) (2022) 262–274, https://doi.org/10.1016/s2468-1253(21)00426-x.
[6] S.F. Roerink, N. Sasaki, H. Lee-Six, M.D. Young, L.B. Alexandrov, S. Behjati, T. J. Mitchell, S. Grossmann, H. Lightfoot, D.A. Egan, A. Pronk, N. Smakman, J. van Gorp, E. Anderson, S.J. Gamble, C. Alder, M. van de Wetering, P.J. Campbell, M. R. Stratton, H. Clevers, Intra-tumour diversification in colorectal cancer at the single-cell level, Nature 556 (7702) (2018) 457, https://doi.org/10.1038/s41586-018-0024-3.
[7] Z. Zhang, Y. Du, X. Shi, K. Wang, Q. Qu, Q. Liang, X. Ma, K. He, C. Chi, J. Tang, B. Liu, J. Ji, J. Wang, J. Dong, Z. Hu, J. Tian, NIR-II light in clinical oncology: opportunities and challenges, Nat. Rev. Clin. Oncol. 21 (6) (2024) 449–467, https://doi.org/10.1038/s41571-024-00892-0.
[8] X. Xu, H. Zhang, Y. Cao, W. Liu, Z. Chen, C. Li, Cell membrane-targeted J-aggregation strategy for synergistic immune checkpoint degradation and immunogenic Pyroptosis to augment tumor immunotherapy, Angew. Chem. Int. Ed. 64 (2025) e202516014, https://doi.org/10.1002/anie.202516014.
[9] H. Zhang, X. Xu, Y. Cao, Z. Chen, W. Liu, X. Lu, C. Li, Unlocking the power of Photothermal agents: a universal platform for smart immune NIR-agonists for precise Cancer therapy, Angew. Chem. Int. Ed. 64 (2025) e202424830, https://doi.org/10.1002/anie.202424830.
[10] M. Lu, S.B. Zhang, M.Y. Yang, Y.F. Liu, J.P. Liao, P. Huang, M. Zhang, S.L. Li, Z. M. Su, Y.Q. Lan, Dual photosensitizer coupled three-dimensional metal-covalent organic frameworks for efficient photocatalytic reactions, Angew. Chem. Int. Ed. 62 (31) (2023), https://doi.org/10.1002/anie.202307632.
[11] Y.W. Wang, J.H. Liao, Y. Lyu, Q.Q. Guo, Z.R. Zhu, X.P. Wu, J.H. Yu, Q. Wang, W. H. Zhu, An AIE photosensitizer with simultaneous type I and type II ROS generation: efficient bacterial elimination and hypoxic tumor ablation, Adv. Funct. Mater. 33 (33) (2023), https://doi.org/10.1002/adfm.202301692.
[12] G. Xu, C.W. Li, C. Chi, L.Y. Wu, Y.Y. Sun, J. Zhao, X.H. Xia, S.H. Gou, A supramolecular photosensitizer derived from an Arene-Ru(II) complex self-assembly for NIR activated photodynamic and photothermal therapy, Nat. Commun. 13 (1) (2022), https://doi.org/10.1038/s41467-022-30721-w.
[13] L. Lv, B. Fan, X. Ji, Y. Liu, T. Chen, Y. Li, X. Gao, P. Chen, B. Tang, G. Chen, From the clinical perspective of photodynamic therapy and photothermal therapy: structure-activity-practice, Coord. Chem. Rev. 507 (2024) 215733, https://doi.org/10.1016/j.ccr.2024.215733.
[14] Y. Kang, X. Ji, Z. Li, Z. Su, S. Zhang, Boron-based nanosheets for combined cancer photothermal and photodynamic therapy, J. Mater. Chem. B 8 (21) (2020) 4609–4619, https://doi.org/10.1039/d0tb00070a.
[15] J. An, S.L. Tang, G.B. Hong, W.L. Chen, M.M. Chen, J.T. Song, Z.L. Li, X.J. Peng, F. L. Song, W.H. Zheng, An unexpected strategy to alleviate hypoxia limitation of photodynamic therapy by biotinylation of photosensitizers, Nat. Commun. 13 (1) (2022), https://doi.org/10.1038/s41467-022-29862-9.
[16] Y. Cao, H. Zhang, Z. Chen, W. Liu, J. Liu, C. Li, Chemiluminescence-powered immunotherapy for deep tumors: promoting PD-L1 degradation and igniting pyroptosis through subcellular trafficking and targeting, Adv. Mater. 38 (2026) e19569, https://doi.org/10.1002/adma.202519569.
[17] H. Lin, Y. Chen, J. Shi, Nanoparticle-triggered in situ catalytic chemical reactions for tumour-specific therapy, Chem. Soc. Rev. 47 (6) (2018) 1938–1958, https://doi.org/10.1039/C7CS00471K.
[18] B.W. Yang, Y. Chen, J.L. Shi, Reactive oxygen species (ROS)-based nanomedicine, Chem. Rev. 119 (8) (2019) 4881–4985, https://doi.org/10.1021/acs.chemrev.8b00626.
[19] B.W. Yang, Y. Chen, J.L. Shi, Nanocatalytic medicine, Adv. Mater. 31 (39) (2019) 1901778, https://doi.org/10.1002/adma.201901778.
[20] X. Lu, S. Gao, H. Lin, J. Shi, Single-atom catalysts for Nanocatalytic tumor therapy, Small 17 (16) (2021) 2004467, https://doi.org/10.1002/smll.202004467.
[21] C.N. Loynachan, A.P. Soleimany, J.S. Dudani, Y. Lin, A. Najer, A. Bekdemir, Q. Chen, S.N. Bhatia, M.M. Stevens, Renal clearable catalytic gold nanoclusters for in vivo disease monitoring, Nat. Nanotechnol. 14 (9) (2019) 883–890, https://doi.org/10.1038/s41565-019-0527-6.
[22] Z. Xu, S.H. Ding, W.D. Shi, W.K. Zhao, X.J. Cao, Z.Y. Yao, Y.X. Guo, G.K. Long, C. X. Li, X.J. Wan, Y.S. Chen, High performance electron acceptors containing transition metals, Angew. Chem. Int. Ed. 64 (23) (2025), https://doi.org/10.1002/anie.202504616.
[23] J.P.A. Souza, L. Benatto, G. Candiotto, L. Wouk, M. Koehler, Dynamics of vibrationally coupled intersystem crossing in state-of-the-art organic optoelectronic materials, Commun. Chem. 8 (1) (2025) 84, https://doi.org/10.1038/s42004-025-01485-3.
[24] H. Yersin, R. Czerwieniec, U. Monkowius, R. Ramazanov, R. Valiev, M.Z. Shafikov, W.-M. Kwok, C. Ma, Intersystem crossing, phosphorescence, and spin-orbit coupling. Two contrasting cu(I)-TADF dimers investigated by milli- to micro-second phosphorescence, femto-second fluorescence, and theoretical calculations, Coord. Chem. Rev. 478 (2023) 214975, https://doi.org/10.1016/j.ccr.2022.214975.
[25] G. Niu, G. Song, Y. Kang, Y. Zhai, Y. Fan, J. Ye, R. Li, R. Li, Y. Zhang, H. Wang, Y. Chen, X. Ji, Quinoidal semiconductor nanoparticles for NIR-II photoacoustic imaging and photoimmunotherapy of cancer, Adv. Mater. 37 (6) (2024), https://doi.org/10.1002/adma.202415189.
[26] T. Li, G. Hu, L. Tao, J. Jiang, J. Xin, Y. Li, W. Ma, L. Shen, Y. Fang, Y. Lin, Sensitive photodetection below silicon bandgap using quinoid-capped organic semiconductors, Sci. Adv. 9 (13) (2023) eadf6152, https://doi.org/10.1126/sciadv.adf6152.
[27] G. Niu, X. Bi, Y. Kang, H. Zhao, R. Li, M. Ding, B. Zhou, Y. Zhai, X. Ji, Y. Chen, An acceptor–donor–acceptor structured Nano-aggregate for NIR-triggered interventional Photoimmunotherapy of cervical Cancer, Adv. Mater. 36 (39) (2024), https://doi.org/10.1002/adma.202407199.
[28] P. Bag, V. Chukhutsina, Z. Zhang, S. Paul, A.G. Ivanov, T. Shutova, R. Croce, A. R. Holzwarth, S. Jansson, Direct energy transfer from photosystem II to photosystem I confers winter sustainability in scots pine, Nat. Commun. 11 (1) (2020) 6388, https://doi.org/10.1038/s41467-020-20137-9.
[29] T. Mirkovic, E.E. Ostroumov, J.M. Anna, R. van Grondelle, Govindjee, G. D. Scholes, Light absorption and energy transfer in the antenna complexes of photosynthetic organisms, Chem. Rev. 117 (2) (2017) 249–293, https://doi.org/10.1021/acs.chemrev.6b00002.
[30] J. Ravensbergen, S. Pillai, D.D. Méndez-Hernández, R.N. Frese, R. van Grondelle, D. Gust, T.A. Moore, A.L. Moore, J.T.M. Kennis, Dual singlet excited-state quenching mechanisms in an artificial Caroteno-Phthalocyanine light harvesting antenna, ACS Phys. Chem. Au 2 (1) (2022) 59–67, https://doi.org/10.1021/acsphyschemau.1c00008.
[31] Z.H. Li, Z.W. Zhou, Y.R. Wang, J. Wang, L.M. Zhou, H.B. Cheng, J. Yoon, Activatable nano-photosensitizers for precise photodynamic cancer therapy, Coord. Chem. Rev. 493 (2023), https://doi.org/10.1016/j.ccr.2023.215324.
[32] T.C. Pham, V.N. Nguyen, Y. Choi, S. Lee, J. Yoon, Recent strategies to develop innovative photosensitizers for enhanced photodynamic therapy, Chem. Rev. 121 (21) (2021) 13454–13619, https://doi.org/10.1021/acs.chemrev.1c00381.
[33] Y. Kang, N. Kong, M. Ou, Y. Wang, Q. Xiao, L. Mei, B. Liu, L. Chen, X. Zeng, X. Ji, A novel cascaded energy conversion system inducing efficient and precise cancer therapy, Bioact. Mater. 20 (2023) 663–676, https://doi.org/10.1016/j.bioactmat.2022.07.007.
[34] X. Yuan, Y. Kang, R. Li, G. Niu, J. Shi, Y. Yang, Y. Fan, J. Ye, J. Han, Z. Pei, Z. Zhang, X. Ji, Magnetically triggered thermoelectric heterojunctions with an efficient magnetic-thermo-electric energy cascade conversion for synergistic cancer therapy, Nat. Commun. 16 (1) (2025), https://doi.org/10.1038/s41467-025-57672-2.
[35] Y. Lin, M.T. Dylla, J.J. Kuo, J.P. Male, I.A. Kinloch, R. Freer, G.J. Snyder, Graphene/strontium Titanate: approaching single crystal-like charge transport in polycrystalline oxide perovskite nanocomposites through grain boundary engineering, Adv. Funct. Mater. 30 (12) (2020), https://doi.org/10.1002/adfm.201910079.
[36] S. Cook, K. Letchworth-Weaver, I.C. Tung, T.K. Andersen, H. Hong, L.D. Marks, D. D. Fong, How heteroepitaxy occurs on strontium titanate, Sci. Adv. 5 (4) (2019), https://doi.org/10.1126/sciadv.aav0764.
[37] C. Richter, M. Zschornak, D. Novikov, E. Mehner, M. Nentwich, J. Hanzig, S. Gorfman, D.C. Meyer, Picometer polar atomic displacements in strontium titanate determined by resonant X-ray diffraction, Nat. Commun. 9 (2018), https://doi.org/10.1038/s41467-017-02599-6.
[38] S. Fan, Y. Jin, X. Ai, S. Gu, E. Song, Q. Zhang, L. Wang, W. Jiang, Enhancing thermoelectric properties of strontium Titanate through in situ growth of carbon nanotubes, Small 21 (18) (2025) 2411022, https://doi.org/10.1002/smll.202411022.

[39] T.N. Pham, B. Andrea Choi Tan, Y. Hamamoto, K. Inagaki, I. Hamada, Y. Morikawa, Stability of PdxOy particles supported on strontium titanate perovskite under three-way catalyst operating conditions: implications for sintering resistance, ACS Catal. 14 (3) (2024) 1443–1458, https://doi.org/10.1021/acscatal.3c05673.

[40] Y. Kang, Z. Li, Y. Yang, Z. Su, X. Ji, S. Zhang, Antimonene Nanosheets-based Z-scheme Heterostructure with enhanced reactive oxygen species generation and Photothermal conversion efficiency for photonic therapy of Cancer, Adv. Healthc. Mater. 10 (2021) 2001835, https://doi.org/10.1002/adhm.202001835.

[41] S. Song, Y. Zhao, M. Kang, F. Zhang, Q. Wu, N. Niu, H. Yang, H. Wen, S. Fu, X. Li, Z. Zhang, B.Z. Tang, D. Wang, An NIR-II excitable AIE small molecule with multimodal Phototheranostic features for Orthotopic breast Cancer treatment, Adv. Mater. 36 (2024) 2309748, https://doi.org/10.1002/adma.202309748.

[42] Z. Wang, Q. Su, W. Deng, X. Wang, H. Zhou, M. Zhang, W. Lin, J. Xiao, X. Duan, Morphology-mediated tumor deep penetration for enhanced near infrared II Photothermal and chemotherapy of colorectal Cancer, ACS Nano 18 (2024) 28038, https://doi.org/10.1021/acsnano.4c07085.